약학 박사 학위논문

Structural and Functional studies of VapBC and SehAB from *Salmonella enterica* Typhimurium LT2

살모넬라균 유래 VapBC 와 SehAB 독소-항독소 단백질의 구조적, 기능적 연구

2019년 2월

서울대학교 대학원

약학과 물리약학전공

박 동 원

Abstract

Structural and Functional studies of VapBC and SehAB from *Salmonella enterica* Typhimurium LT2

Dong Won, Park

College of Pharmacy

Seoul National University

Bacterial toxin–antitoxin (TA) system has gained attention for its essential roles in cellular maintenance and survival under harsh environmental conditions such as nutrient deficiency, antibiotic treatment and oxidative stress. The TA systems are generally classified into six types, according to the structure of antitoxin or mode of inhibition toxin activity by antitoxin. Among them, type 2 TA systems are the most studied. The type II TA system is composed a

labile antitoxin and a stable toxin. Under normal environments, the antitoxin protein binds to its cognate toxin and forms a stable complex to inhibit the toxic effects. However, under stressful environments accompanying with oxidative stress, temperature changes, starvation caused by malnutrition, and treatment of antibiotics, kinds of proteases which were produced by host cells degrade the antitoxin molecules and allow its cognate toxin to be released. This situation can lead to deaths or growth inhibition of the host cells. All type II TA operons are autoregulated at the transcriptional level by antitoxins, which bind to TA locus promoters. Type II antitoxin usually has a DNA-binding domain at the N-terminus of the protein, while the C-terminus of the antitoxin protein interacts with cognate toxin. This DNA-binding domain has a domain such as RHH (Ribbon-Helix-Helix), HTH (Helix-Turn-Helix), PhD like-, or AbrB-like domain.

There are at least 14 type II TA systems in *Salmonella enterica* serovar Typhimurium LT2, one of pathogenic bacteria, and none of their structures have been determined. We determined the crystal

structure of the VapBC TA complex from *S.* Typhimurium LT2 in DNA-free and -bound forms at 2 Å and 2.8 Å resolution, respectively. The VapC toxin possesses a PIN-domain that shows metal dependent ribonuclease activity. The PIN domain has four acidic residues that form a negatively charged cavity. We were identified VapC from *S.* Typhimurium LT2 as a putative Ca^{2+}-dependent ribonuclease using a fluorescence quenching assay, which is discriminated from previous data showing that VapC homologs have Mg^{2+} or Mn^{2+}-dependent ribonuclease activities. The $VapB_{LT2}$ possesses a Abr-B type DNA binding domain which is regulate transcription of $VapBC_{LT2}$.

Additionally, we revealed the crystal structure of the SehAB TA complex from *S.* Typhimurium at 2.49 Å resolution. SehA toxin shares RelE toxin protein features that shows ribosome dependent ribonuclease activity. The SehA toxin is expected to show ribonuclease activity also. As a result of measuring ribonuclease activity of SehA toxin, we could reveal that C-terminal alpha helix of SehA toxin have a significant effect on toxin activity. The SehB

antitoxin has a Helix Turn Helix-type DNA binding domain on the C-terminal. Based on the structure, we can see the way SehB antitoxin inhibits SehA toxin. The DNA-bound and -free VapBC structures revealed details of interaction mode between VapBC and the cognate promoter DNA, including the steric inhibition of the VapC active site by VapB and the linear conformation of bound DNA in the VapBC complex. It also revealed the first VapC toxin that showed Ca^{2+}-dependent ribonuclease activity. We could observe the unique SehA toxin and SehB antitoxin binding mode through the SehAB complex structure and found the factors affecting the activity of SehA toxin. Salmonella has spread to many countries where economic development is slow to this day, and resistance to existing antibiotics is also increasing. Therefore, the development of new antibiotics is expected to be of great help in the treatment of *Salmonella*. The three toxin - antitoxin complexes identified in this study provided the binding and structural information of the toxin-antitoxin, and the structural features and functions of the toxin-antitoxin described in this study will be a cornerstone in the development of new antibiotic

candidates.

Key words: Toxin-Antitoxin, DNA-protein complex, antibiotic peptide, Ca^{2+}

Student number: 2014-30569

Table of Contents

List of Tables

List of Figures

Introduction

Bacterial toxin–antitoxin (TA) systems have received increasing attention for their diverse identities, structures, and functional implications in cell cycle arrest and survival against environmental stresses such as nutrient deficiency, antibiotic treatments, and temperature changes. TA operons were first identified on the mini-F plasmid of Escherichia coli as important genetic elements responsible for cell survival; after cell division, only the daughter cell that harbour the TA genes on the transferable plasmid survives (1,2). In other words, if the daughter cell does not inherit the plasmid which contains TA gene, then in the stressed environment, the unstable antitoxin in the existing TA complex is degraded and the cell is killed by the toxin. TA systems are typically encoded in operons that are located on bacterial plasmids and chromosomes. TA system exists as a stable complex in normal environment. However, as mentioned above, relatively unstable antitoxin is degraded by specific protease when exposed to a stress environment, and thus the free toxin

degrades RNA or inhibits DNA gyrase activity and the like, thereby killing the cells or inhibiting cell growth. The mechanism and characteristic of such TA system are attracting attention as a target of a new antibiotic candidate.

Salmonella is a Gram-negative bacteria and is divided into the pathogenic strain *Samonella eneterica* and the non-pathogenic strain *Salmonella bongori*. Among *Salmonella enterica* strains, strains that caused typhoidal fever and other strains caused non-typhoidal fever (3). *Salmonella* infection is one of the major diseases spread in developing or low income countries (4,5). The International Vaccine Institute estimated that there were 11.9 million typhoid fever illnesses and 129,000 deaths in low- and middle-income countries in 2010 (5). Traditional first-line antibiotics of *Salmonella* include chloramphenicol, amoxicillin and trimethoprim-sulfamethoxazole (3,6,7). *Salmonella* strains, however, have resistance to these drugs called Multi Drug Resistance (MDR). The emergence of MDRs required new antibiotics, followed by 3rd generation cephalosporin, fluoroquinolones, and azithromycin (3). However, antibiotic

resistances of these antibiotics were also found. Therefore, the development of new antibiotics is necessary, and the TA system as a target for new antibiotics will be a good option. There are at least 16 type II TA systems in *Salmonella enterica* serovar Typhimurium LT2, one of pathogenic bacteria (Table 1). Among them, two TA pairs were selected for structural and functional research. The first TA pair is the STM3033 VapC toxin and the STM3034 VapB antitoxin pair, the second TA pair is the STM4030 SehB antitoxin and the STM4031 SehA toxin pair. Although functional studies of these pairs had progressed partially, structural studies have not been carried out, so they have been selected as research subjects. The STM3033-STM3034 VapBC pair has been under studying for the activity of VapC toxin and VapB antitoxin, and studies of the VapBC pair from other organisms have also been actively conducted, but there is no study of the structure of VapBC from *Salmonella* (8-10). The STM4030-STM4031 pair was also selected as a research subject, because there was only a part of the activity but no structural and functional study (11). The goal of this study is to devise antibiotic

candidates based on the results obtained by identifying their structure and function.

Table 1. List of type II Toxin-Antitoxin system in *Salmonella eneterica* serovar Typhimurium LT2

	Toxin	Antitoxin	Classification(family/domain)
1	STM1550	STM1551	relBE/PHD-RelE
2	STM2905	STM2904	-/RHH-GNAT
3	STM2954	STM2955	RelBE or parDE */RHH-RelE
4	STM3033	STM3034	vapBC/AbrB-PIN
5	STM3470	STM3471	-/YhfG-Fic
6	STM3516	STM3517	relBE/RHH-RelE
7	STM3558	STM3559	phd-doc/PHD-Fic
8	STM3651	STM3652	-/RHH-GNAT
9	STM3777	STM3778	relBE */Xre-RelE
10	STM3906	STM3907	higBA/COG5606-RelE
11	STM4031	STM4030	relBE */Xre-RelE
12	STM4032	STM4033	relBE */Xre-RelE
13	STM4318	STM4317	-/RHH-GNAT
14	STM4450	STM4449	relBE/RHH-RelE
15	STM4528	STM4529	-/RHH-COG2929
16	STM4528	STM4529	-/RHH-COG2929

Chapter 1. Crystal structure of DNA-free and -bound VapBC from *Salmonella* Typhimurium LT2 and VapC as a putative Ca^{2+}-dependent ribonuclease

1.1. Introduction

TA operons were first discovered on the mini-F plasmid of *Escherichia coli* in 1983, and had an important role in maintenance of host bacteria (2). After cell division, daughter cells that have plasmid encoding TA operons survive. When a daughter cell lost the parental plasmid coding TA operons, daughter cells were killed by the toxin which released from the TA complex caused by degradation of labile antitoxin (1). Since the first discovery of TA operons from prokaryotes, TA operons in various bacterial chromosomes have been reported (1), and identification of the abundance of TA operons on the chromosome of prokaryotes has generated the idea that TA operons might have other biological roles, such as multidrug

tolerance (12−14), biofilm formation (15), and arrest of cellular growth (16) under harsh conditions, such as nutrient deficiency, antibiotic treatment, bacteriophage infection, immune system attack, oxidative stress, and high temperature (17,18). The TA pairs are generally classified into six types, according to the genetic structure and regulation modes of antitoxin molecules (19−21). In the type I and III TA systems, the antitoxins are RNA molecules, that directly inhibit translation or regulate toxin activities. In the type I TA system, antitoxins as unstable antisense RNAs directly bind to mRNA molecules of toxin. Type I toxin and antitoxin genes are transcribed from their own promoters, whereas other type TA operons are commonly cotranscribed from a single promoter of the TA operons (22,23). In contrast to the type I TA system, the type III TA system is composed of the protein toxin and the RNA antitoxin. Type III RNA antitoxin binds to protein toxin to inhibit toxin activities. TA systems of types IV, V and VI were newly reported (24−26). In both type IV and V TA systems, the antitoxin functions as a protein. In the type IV TA system, antitoxins bind to target proteins of type IV toxin to

stabilize the target protein, leading to suppression of the activities of the toxin (26). In the type V TA system, antitoxin degrades mRNAs of toxins and inhibits translation of type V toxins (24). In type VI TA system, the type VI toxin SocB is unstable and degraded by the protease ClpXP, but toxin degraded by ClpXP needs the proteolytic adaptor antitoxin SocA (25). The type II TA system is composed a labile antitoxin and a stable toxin. Under normal environments, the antitoxin protein binds to its cognate toxin and forms a stable complex to inhibit the toxic effects (27). When bacterial cells encounter harsh conditions, stress-induced proteases degrade the labile antitoxin and allow its cognate toxin to be released. This situation can lead to the death or growth inhibition of the host cells (28-30). The most abundant type II family is the VapBC family, for instance, at least 50 and 26 VapBC genes are present in *Mycobacterium tuberculosis* and *Sulfolobus solfataricus,* respectively (31-33). VapC toxins contain a pilT N-terminal domain (PIN-domain), which possesses canonical $\alpha/\beta/\alpha$ sandwich structures and four conserved catalytic acidic residues although their sequence

identity is low (34). PIN-domain proteins share structural homology with the T4 RNase H nuclease domain (35). Many studies recently confirmed that VapC toxin has ribo- or deoxyribonuclease activities *in vitro* (8,34,36,37). All type II TA operons are autoregulated at the transcriptional level by antitoxins, which bind to TA locus promoters. Type II antitoxin usually has a DNA-binding domain at the N-terminus of the protein, while the C-terminus of the antitoxin protein interacts with cognate toxin. This DNA-binding domain has a domain such as RHH (Ribbon-Helix-Helix), HTH (Helix-Turn-Helix), PhD like-, or AbrB-like domain. (38,39). There are at least 14 type II TA complexes from *Salmonella enterica* serovar Typhimurium LT2 (11,40). Two type II TA complexes from *S.* Typhimurium show effectiveness *in vivo* (8,9,11). Recent studies have shown that TA complexes could be potent targets of antibacterial peptides (41,42). In this work, we solved the crystal structures of the VapBC complex from *S.* Typhimurium LT2 in DNA-free and -bound states at 2 Å and 2.8 Å, respectively. The structures revealed critical residues of the VapB antitoxin for binding to the VapC toxin and DNA, which may

contribute to an understanding of the transcriptional repression of VapBC systems from *S.* Typhimurium. We also identified the VapC toxin as a Ca^{2+}−dependent ribonuclease using a fluorescence assay, which was not found in other VapC homologs.

1.2. Materials and Methods

1.2.1. Cloning, expression, and protein purification

The primers used in the study are listed in Table 1. The genes used in this study were amplified by polymerase chain reaction (PCR). The amplified DNA was inserted into an expression vector that had been digested with both NdeI and XhoI. Each plasmid was then transformed into *E. coli* DH5α competent cells. The resulting inserted genes were verified by DNA sequencing. The gene coding for $VapC_{LT2}$ (STM3033) from *S.* Typhimurium LT2 was cloned into the expression vector pET21a(+), which allows the production of $VapC_{LT2}$ in an intact form. The gene coding for $VapB_{LT2}$ (STM3034) from *S.* Typhimurium LT2 was cloned into the expression vector

pET28a(+), which allows the production of an N-terminal hexahistidine tag. Both recombinant plasmids ($VapC_{LT2}$: pET21a(+), $VapB_{LT2}$: pET28a (+)) were cotransformed into *E. coli* BL21(DE3) cells. The cells were grown at 37° C in Luria broth (LB) medium supplemented with ampicillin and kanamycin until the OD_{600} reached 0.5. Expression was induced by the addition of 0.5 mM isopropyl 1-thio-β-D-galactopyranoside (IPTG), and the culture was grown at 37° C for 4 h. The cells were harvested by centrifugation at 5,600 ×*g*, lysed by sonication in buffer A (50 mM Tris-HCl at pH 7.9 and 500 mM NaCl) containing 10% (v/v) glycerol, and then centrifuged to remove cellular debris at 17,900 g. The supernatant was filtered by a 0.45 μm pore size membrane (Millex-HV filter unit, Millipore, USA) to remove remnant debris and facilitate purification. The filtered supernatant was applied to a HiTrap chelating column (GE Healthcare) that was previously equilibrated with buffer A. Both VapB and VapC proteins were eluted with a linear gradient of 0.0-0.5 M imidazole in buffer A. The purified VapBC complex protein (3.65 mg/ml) was incubated with trypsin at 25° C at a protein:protease

ratio of 100:1 (w/w). After 1 h 30 min of trypsin treatment, the trypsin was then removed by a HiLoad 16/60 Superdex 200 prep-grade column (GE Healthcare) that was previously equilibrated with buffer B (50 mM Tris-HCl at pH 7.9 and 300 mM NaCl). For crystallization, the purified protein was concentrated to 3 mg/ml using an Amicon Ultra15 centrifugal filter unit (Millipore). For ribonuclease assays, the gene coding for $VapC_{LT2}$ (STM3033) was cloned into expression vector pET28a (+), which allows the production of $VapC_{LT2}$ with an N-terminal hexahistidine tag. Plasmids containing the $VapC_{LT2}$ gene were then transformed into *E. coli* BL21(DE3) cells. The cells were grown at 37° C in LB medium supplemented with kanamycin until the OD_{600} reached 0.5. Protein expression was induced by the addition of 0.5 mM isopropyl 1-thio-β-D-galactopyranoside (IPTG), and the culture was grown at 37° C for 4 h. The cells were harvested by centrifugation at 5,600 x*g*, lysed by sonication in buffer A (50 mM Tris-HCl at pH 7.9 and 500 mM NaCl) containing 10% (v/v) glycerol and then centrifuged to remove cellular debris at 17,900 g. The supernatant was filtered by

a 0.45 μm pore size membrane (Millex-HV filter unit, Millipore, USA) to remove remnant debris and facilitate purification. The filtered supernatant was applied to a HiTrap chelating column (GE Healthcare) that was previously equilibrated with buffer A, and the eluted sample was further purified by size-exclusion chromatography using a HiLoad 16/60 Superdex 75 prep-grade column (GE Healthcare) that was previously equilibrated with buffer B. EDTA treatment and a dialysis process for the ribonuclease assay are described below. For DNA-bound $VapBC_{LT2}$ cocrystallization, the growth conditions and the first purification step were identical to those of proteolyzed $VapBC_{LT2}$. The eluted $VapBC_{LT2}$ from the HiTrap chelating column sample was further purified by size-exclusion chromatography using a HiLoad 16/60 Superdex 200 prep-grade column (GE Healthcare) that was previously equilibrated with buffer C (20 mM Tris-HCl at pH 7.9 and 150 mM NaCl). Oligonucleotides for crystallization were annealed by heating to 94°C for 5 min and then cooling to 4°C in DDW. The sequence of the forward oligonucleotide was 5 -CCTGTATATCTCTTTGACATATACATC-

3. $VapBC_{LT2}$ was mixed with duplex DNA in a 1:4 molar ratio, incubated for 30 min at room temperature and purified by gel filtration in a preparative Superdex 200GL 10/300 column that was previously equilibrated with buffer D (20 mM Tris–HCl at pH 7.9 and 75 mM NaCl).

Table 1. Primer used for $VapBC_{LT2}$ TA system

	sequence (5' – 3')
$VapC_{LT2}$_F	GCGGTCATATGCTGAAATTCATGCTTGATACCAA
$VapC_{LT2}$_R	GATTACCGCTCGAGTTAGCACCAGTCTTCGATTCGG
$VapB_{LT2}$_F	GCGGTCATATGCACACAACACTTTTTTTTAGTAA
$VapB_{LT2}$_R	GCGGTCCGCTCGAGTTAAAATCCTTCCCGTTCCTGTA
DNAI_F	CCTGTATATCTCTTTGACATATACATC
DNAII_F	AATGGATATACGCGTTGTATATCCAGA
$VapC_{LT2}$ Substrate	UCAUAACCCGAAGA

1.2.2. Crystallization and X-ray data collection

Crystallization of DNA-free $VapBC_{LT2}$ and the DNA-bound $VapBC_{LT2}$ complex was performed at 20°C by the sitting-drop vapor diffusion method. Each sitting drop was prepared by mixing equal volumes (1 μl each) of the protein solution and the reservoir solution. Structure-solved crystals of DNA-free $VapBC_{LT2}$ were obtained with a reservoir solution of 0.2 M lithium sulfate, 0.1 M CAPS/sodium hydroxide at pH 10.5 and 2 M ammonium sulfate. The best crystals of the DNA-bound $VapBC_{LT2}$ complex were obtained with a reservoir solution of 0.2 M ammonium citrate tribasic dehydrate, pH 7, and 20% (w/v) PEG3350. The crystals of both DNA-free $VapBC_{LT2}$ and DNA-bound $VapBC_{LT2}$ were transferred to a cryoprotectant solution that contained 20% (v/v) glycerol in the reservoir solution. X-ray diffraction data for crystals were collected at 100 K using a Pilatus 6M (Dectris, Switzerland) detector at the BL-5C experimental station of Pohang Light Source, Korea and EIGER X 16 M detector (Dectris, Switzerland) at the beamline BL44XU, SPring-8, Japan. For each image, the crystal was rotated

by 1° and the raw data were processed and scaled using the program suit HKL2000 and XDS (43,44). The crystals of DNA-free $VapBC_{LT2}$ LT2 belong to space group $P2_1$ with unit cell dimensions of a = 53.956 Å, b = 114.942 Å, and c = 53.998 Å. The crystals of DNA-bound $VapBC_{LT2}$ also belong to space group $P3_1$ with unit cell dimensions of a = 93.677 Å, b = 93.677 Å, and c = 122.440 Å.

1.2.3. Structure determination and refinement

The DNA-free $VapBC_{LT2}$ structures were determined by molecular replacement using isolated VapBC complexes from *Shigella flexneri* with the PDB code 3TND as a search model. The DNA-bound $VapBC_{LT2}$ structure was determined by molecular replacement using isolated DNA-free $VapBC_{LT2}$ as a search model. Both structures were manually rebuilt in Coot and iteratively refined with CCP4. Water molecules were added using the program Coot and were manually added. Then, 96.4% and 92.4% of the residues in the models from DNA-free $VapBC_{LT2}$ and DNA-bound $VapBC_{LT2,}$ respectively, were found to lie in favored regions of the Ramachandran plot.

Solvent-accessible surface areas were calculated using *PISA* (45). Electrostatic surface potentials were calculated using the CHARMM force field implemented in the server-based version of PDB2PQR (46). The resulting PQR file was used to calculate and display the electrostatic surface potential using the APBS method (47). The refined model was visualized and drawn using PyMOL (48). Crystallographic and refinement statistics are summarized in Table 2.

Table 2. Statistics for data collection and model refinement

Data set	Apo form	DNA bound form
A. Data collection		
X-ray source	PLS5C	SPring-8 44XU
X-ray wavelength (Å)	0.97960	0.9
Space group	$P2_1$	$P3_1$
Unit cell length (a, b, c, Å)	54.0 114.8 54.0	93.7 93.7 122.4
Unit cell angle (α, β, γ, °)	90, 114.3, 90	90, 90, 120
Resolution range (Å)	50.0–2.00 (2.03–2.00)[a]	50–2.8 (2.97–2.80)[a]
Total / unique reflections	171,214 / 38,160	172,916 / 58,287
Completeness (%)	93.9 (99.8)[a]	99.0 (97.9)[a]
Average I/σ (I)	26.3 (4.7)[a]	13.3 (1.9)[a]
R_{merge}[b] (%)	9 (31.8)[a]	5.2 (53.8)[a]
B. Model refinement		
Resolution range (Å)	57.4–1.99	50.0–2.80
R_{work} / R_{free}[e] (%)	17.5 / 23.8	20.6 / 23.3
Monomers per asymmetric unit	8	8
Number of non-hydrogen atoms / average B-factor (Å^2)		
Protein	4,976 / 36.7	6,340 / 25.6
Water oxygen	206 / 39.5	149 / 24.1
Calcium ion	4/ 81.5	
DNA		1107 / 53.9
R.m.s. deviations from ideal geometry		
Bond lengths (Å) / bond angles (°)	0.016 / 1.59	0.008 / 1.09
Protein-geometry analysis		
Ramachandran favored (%)	96.4	92.4
Ramachandran allowed (%)	3.1	6.6
Ramachandran outliers (%)	0.5	1
PDB code	6IFC	6IFM

1.2.4. *In vitro* ribonuclease assay

The ribonuclease activity of $VapC_{LT2}$ and its metal dependence were assessed by a fluorescence quenching assay using fluorescence-labeled synthetic oligoribonucleotides (14 bases) (5 - UCAUAACCCGAAGA-3) as a substrate. Basically, a fluorophore is connected to one end of the synthetic RNA strand and quenched by the neighboring quencher group at the other end. When ribonuclease is added to the synthetic RNA containing fluorophore and quencher, digestion of the RNA provokes an increase in fluorescence at 520 nm after excitation at 490 nm by a light source. Specifically, we used 6-carboxyfluorescein (FAM) as a fluorophore in these assays. A 6-FAM fluorophore was covalently linked to the end of the synthetic RNA molecule and quenched by a Black Hole Quencher (BHQ) group linked on the other end. We first screened the metal-dependent ribonuclease activity of $VapC_{LT2}$ for several metals such as Ca^{2+}, Cd^{2+}, Co^{2+}, Mg^{2+}, Mn^{2+}, and Zn^{2+}. $VapC_{LT2}$ was pretreated with 30 mM EDTA in buffer A to remove unintended metals that may have been bound during purification. This metal binding ability of $VapC_{LT2}$ was

then regenerated by serial dialysis and size exclusion chromatography against buffer B. Before the assay, $VapC_{LT2}$ and $VapBC_{LT2}$ were preincubated with metal ions at room temperature for 30 min. For the assay, $VapC_{LT2}$ (10 μM), $VapBC_{LT2}$ (10 μM), and the metals (100 μM) were included in a 50 μl reaction solution in buffer B. To determine the optimal Ca^{2+} concentration for the ribonuclease activity of $VapC_{LT2}$, we added varying amounts of Ca^{2+} ions (10 μM, 100 μM, 1 mM, 10 mM and 30 mM) to 10 μM $VapC_{LT2}$ and $VapBC_{LT2}$ proteins. The subsequent fluorescence was recorded at 520 nm after excitation at 490 nm every 30 seconds for 1 h. The negative control contained only 1 mM metal ions in buffer B.

1.2.5. Inductively coupled plasma mass spectrometry

Inductively coupled plasma mass spectrometry was conducted to confirm whether Ca^{2+} was copurified with the $VapBC_{LT2}$ complex. The purified $VapBC_{LT2}$ used in this measurement was eluted from a HiTrap chelating column with a linear gradient of 0.0–0.5 M imidazole in buffer A. An aliquot of the same buffer was used as a control. ELAN

6100, Nex-ION 350D (Perkin-Elmer, USA) and argon plasma (6,000 K) were used for the detection. The radio frequency power was 1,100 W, and the sample injection flow rate was 1 ml/min.

1.2.6. Fluorescence polarization assay

The 5-FAM-labeled 27 bp double-stranded DNA (DNA I & II) of the promoter region was purchased from Bioneer (www.bioneer.com). To compare binding affinities between two DNA sequences, a 100 nM solution of the 5-FAM-labeled DNA was incubated with increasing amounts of the purified proteins in buffer C for 30 min at 25° C. The fluorescence polarization signals were recorded using black 384-well plates (Greiner) on a SpectraMax M5e microplate reader (Molecular Devices) with a 490 nm excitation filter and a 520 nm emission filter. The data were analyzed with Kaleidagraph (Synerge Software).

1.3 Results and Discussion

1.3.1 Overall architecture of $VapBC_{LT2}$ complex

We tried to determine the crystal structure of the VapBC complex from *S.* Typhimurium LT2. However, the complex failed to crystallize in the intact form, possibly due to the presence of flexible regions in the $VapB_{LT2}$ antitoxin. To overcome this obstacle, we randomly removed the flexible regions by limited proteolysis. As shown in the electron density map, limited proteolysis resulted in the removal of the N-terminal domain of $VapB_{LT2}$, which is known to be responsible for DNA binding. The structure of the DNA-free $VapBC_{LT2}$ complex was determined to a resolution of 2 Å by molecular replacement using the structure of the *S. flexneri* VapBC complex (PDB code 3TND) as a search model (49). The structure of the DNA-free $VapBC_{LT2}$ complex was refined to R_{work}/R_{free} values of 0.175/0.238. The space group of the $VapBC_{LT2}$ crystal is $P2_1$ with two heterotetramers. Each $VapC_{LT2}$ homodimer is flanked by two $VapB_{LT2}$ monomers in the asymmetric unit (Figure. 1). The $VapBC_{LT2}$ complex includes a total

of 528 amino acid residues from the $VapC_{LT2}$ toxin (residues 1–132 for chain A, C, E and G), 100 amino acid residues from the $VapB_{LT2}$ antitoxin (residues 40–67 for chains D and H, residues 46–67 for chain B and F), and 206 water molecules. The $VapBC_{LT2}$ complexes have interface areas of 1,240 $Å^2$ (chains A and B), 1,340 $Å^2$ (chains C and D), 1,280 $Å^2$ (chains E and F) and 1,440 $Å^2$ (chains G and H). The difference in the interface areas was mainly explained by the observed differences in the electron densities of $VapB_{LT2}$ chains; the residues Ile40–Pro67 (Ser46 – Pro67) are in chains D and H (chains B and F). We searched the structural homologs of the $VapBC_{LT2}$ complex using the DALI server: the most similar structural homologs were (i) VapBC from *S. flexneri* (49) [PDB code 3TND, Z–scores of 25.6, sequence identity of 78% and VapB4C4 stoichiometry in asymmetric unit]; (ii) VapBC2 from *Rickettsia felis* (50) [PDB code 3ZVK, *Z*–scores of 22.5, sequence identity of 38%, VapB4C4 in asymmetric unit]; (iii) VapBC1 from *Caulobacter crescentus* (51) [PDB code 5L6L, *Z*–scores of 18.4, sequence identity of 25% and VapB4C4 in asymmetric unit]; (iv) FitAB from *Neisseria*

gonorrhoeae (52) [PDB code 2H1C, *Z*−scores of 17.9, sequence identity of 22% and FitA4B4 in asymmetric unit] and (v) VapBC15 from *Mycobacterium tuberculosis* (53) [PDB codes 4CHG, *Z*−scores of 16.3, sequence identities of 20% and VapB4VapC6 in asymmetric unit]. Notably, the sequence similarity shared by the $VapBC_{LT2}$ complex and the homologs, except for *S. flexneri* VapBC, are low (54). Most of the VapBC complexes, including $VapBC_{LT2}$, showed the same stoichiometry, with two VapB2C2 in the asymmetric unit, while VapBC15 from *M. tuberculosis* showed a mixture of VapB2C2 and VapBC2 in the asymmetric unit.

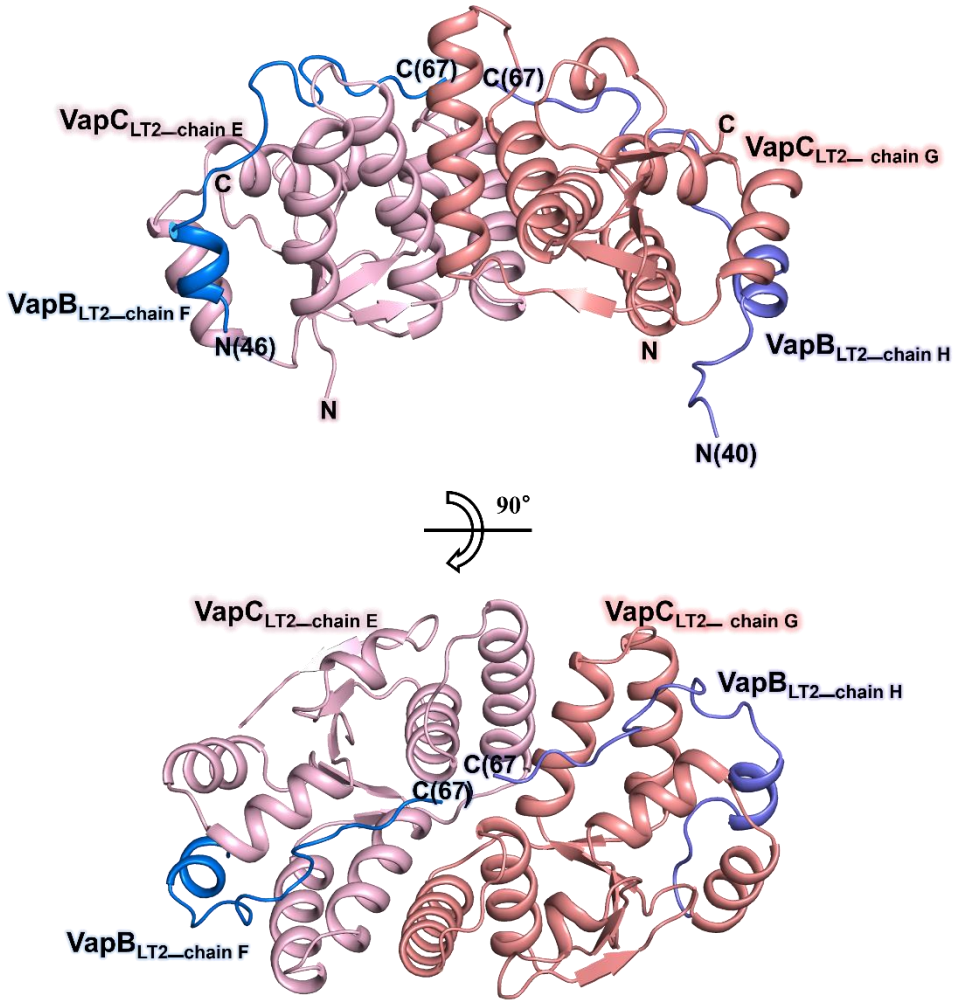

Figure 1. Overall structure of *Salmonella* Typhimurium LT2 DNA−free $VapBC_{LT2}$ in complex. Two orthogonal views of the heterotetrameric DNA−free $VapBC_{LT2}$ complex. Ribbon representation of the $VapBC_{LT2}$ heterotetramer of the crystal. The models of the $VapC_{LT2}$ toxin are shown as salmon and light pink (chains E and G, respectively). The models of the $VapB_{LT2}$ antitoxin are shown as blue and light purple (chain F and H, respectively).

1.3.2 Structure of $VapC_{LT2}$ toxin

The $VapC_{LT2}$ toxin adopts an $\alpha/\beta/\alpha$ fold constituted mainly by five antiparallel β-strands with a topology of $\beta3\uparrow-\beta2\uparrow-\beta1\downarrow-\beta4\downarrow-\beta5\downarrow$; one side is flanked by four α-helices ($\alpha1$ – $\alpha4$), and the other side by three α-helices ($\alpha5$ – $\alpha7$). The $VapC_{LT2}$ homodimer has an average surface area of 1,110–1,130 $Å^2$ per monomer, representing approximately 14% of the total surface of the toxin. Overall, the homodimer of $VapC_{LT2}$ is formed mainly by three interactions between two protomers: interactions between (i) $\alpha3$ and $\alpha5$ helices and between (ii) $\alpha6$ and $\alpha6$ helices, and (iii) interactions of the $\alpha5$ – $\beta3$ loop with the $\alpha3$ helix and $\alpha5$ – $\beta3$ loop (Figure 2A). The residues forming hydrophilic and hydrophobic interactions within the $VapC_{LT2}$ interface are schematically described in Figure 3. Specifically, there are hydrophobic interactions of (i) Ile38, Leu40, Met41, Ile44, and Tyr45 on $\alpha3$ with Ala77, Ile78, Ala85, and Ala88 on $\alpha5$ of the opposing protomer, (ii) Tyr72 on the $\alpha5-\beta3$ loop with Tyr72 on the $\alpha5$ – $\beta3$ loop and Ile38 and Met41 on $\alpha3$, and (iii) Pro96, Tyr97 and Met100 on $\alpha6$ with the same

residues on the opposing $\alpha 6$ (Fig. 2B). There are hydrophilic interactions of (i) Ser37, Met41, and Glu48 on $\alpha 3$ with Gln82, and Arg84 on $\alpha 5$ of the opposing protomer, (ii) Asp71 on the $\alpha 5 - \beta 3$ loop with Thr74 on the $\alpha 5 - \beta 3$ loop, Tyr72 on the $\alpha 5 - \beta 3$ loop with Ser37 on $\alpha 3$ and Tyr72 on the $\alpha 5 - \beta 3$ loop, and (iii) Tyr97 and Gln99 on $\alpha 6$ with the same residues on the opposing $\alpha 6$ (Figure 2C). $VapC_{LT2}$ dimerization might be driven mainly by hydrophobic interactions within the dimer interface because the number of residues involved in hydrophobic interactions is larger than the number of residues involved in hydrophilic interactions.

In a previous study of the interaction between $VapBC_{LT2}$ and DNA, it was suggested that dimerization of $VapC_{LT2}$ would affect the interaction between $VapBC_{LT2}$ and DNA, and so they mutated several residues that are thought to be involved in dimerization of $VapC_{LT2}$ (10). Based on the former mutation analysis, the transcriptional level of $VapBC_{LT2}$ markedly increased when Tyr72 of $VapC_{LT2}$ was mutated, indicating that the mutation causes a weakening of the interaction between $VapBC_{LT2}$ and DNA. One possibility is that the mutation

reduces the dimerization of $VapC_{LT2,}$ which is required for the formation of the $VapBC_{LT2}$–DNA complex. This is consistent with our structure, where Tyr72 is an important residue in the dimerization of $VapC_{LT2}$. Additionally, the residue corresponding to Tyr72 of $VapC_{LT2}$ is conserved in homologs such as VapC from *S. flexneri* (Tyr72), VapC1 from *C. crescentus* (Phe71), VapC2 from *R. felis* (Phe73) and FitB from *N. gonorrhoeae* (Phe78) (Figure 4). Their studies also indicated that conserved aromatic residues play a crucial role in dimerization (50,51,55,56).

We searched for the structural homologs of $VapC_{LT2}$ using the DALI server which gave several matches, all of them VapCs from various organisms (54). The most similar homologs were (i) toxin VapC from *S. flexneri* (49) [PDB code 3TND, Z–scores of 25.6, and sequence identity of 78%]; (ii) toxin VapC from *R. felis* (50) [PDB code 3ZVK, *Z*–scores of 22.3, and sequence identity of 38%]; (iii) toxin VapC from *C. crescentus* (51) [PDB code 5L6L, *Z*–scores of 18.4, and sequence identity of 25%]; (iv) toxin FitB from *N. gonorrhoeae* (52) [PDB code 2H1C, *Z*–scores of 17.9, and sequence

identity of 22%]; (v) toxin VapC−15 from *M. tuberculosis* (53) [PDB codes 4CHG, *Z*−scores of 16.3, and sequence identities of 20%]; and (vi) toxin VapC30 from *M. tuberculosis* (42) [PDB codes 4XGR, Z−scores 15.9, sequence identity of 11%]. The homologs show a high structural similarity to $VapC_{LT2,}$ although the sequence identity is not significant except for that of *S. flexneri* VapC.

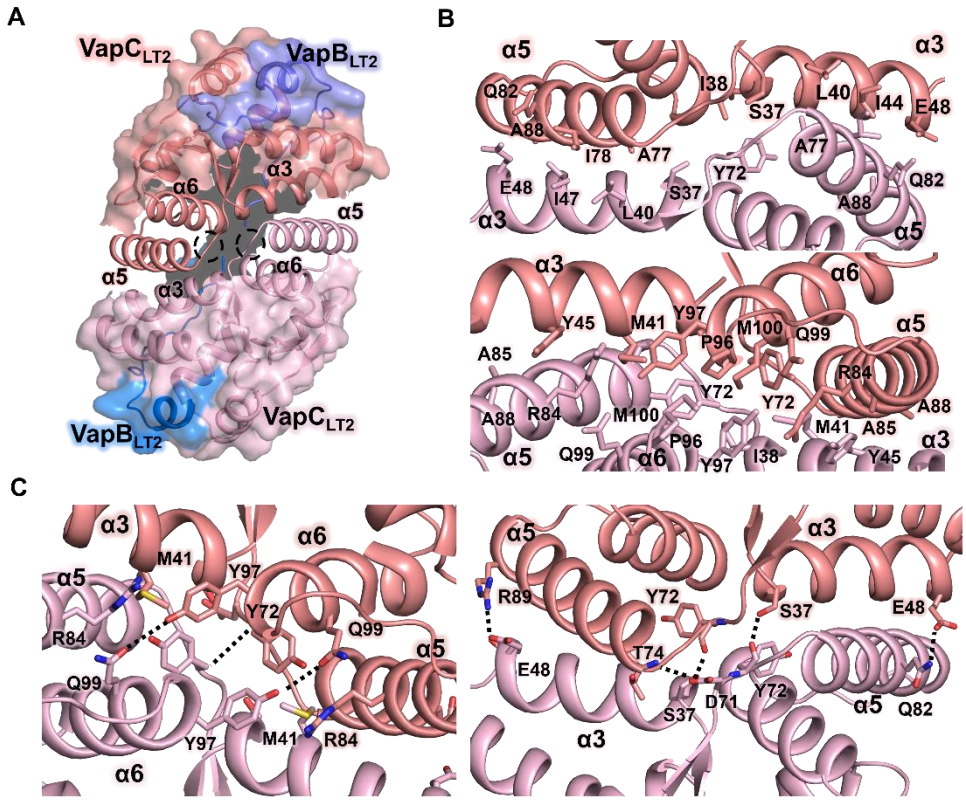

Figure 2. Analysis of the VapC$_{LT2}$ toxin homodimeric interactions. (A) The homodimeric interface of VapC$_{LT2}$ is indicated by a ribbon representation, and the other part is expressed by a semi-transparent surface representation. The $\alpha 5-\beta 3$ loop of VapC$_{LT2}$ is indicated by the black dotted circle. (B) Details of the hydrophobic interaction of the VapC$_{LT2}$ homodimer. Upper: the residues involved in the hydrophobic interactions at the homodimer interfaces. Lower: the residues involved in the hydrophobic interactions at the homodimer interface. Rotation of the upper figure by 180° in the y-axis. (C) Details of the hydrophilic interactions of the VapC$_{LT2}$ homodimer. Left: the residues involved in the hydrophilic interactions at the homodimer interfaces. Right: the residues involved in the hydrophilic interactions at the homodimer interface. Rotation of the left figure by 180° in the y-axis. Hydrogen bonds and salt bridges are shown as the black dotted lines, and the

residues participating in the interactions are shown in the stick models. $VapB_{LT2}$ and $VapC_{LT2}$ are colored as in Figure 1. For simplicity, one-letter codes are used for the amino acid labels.

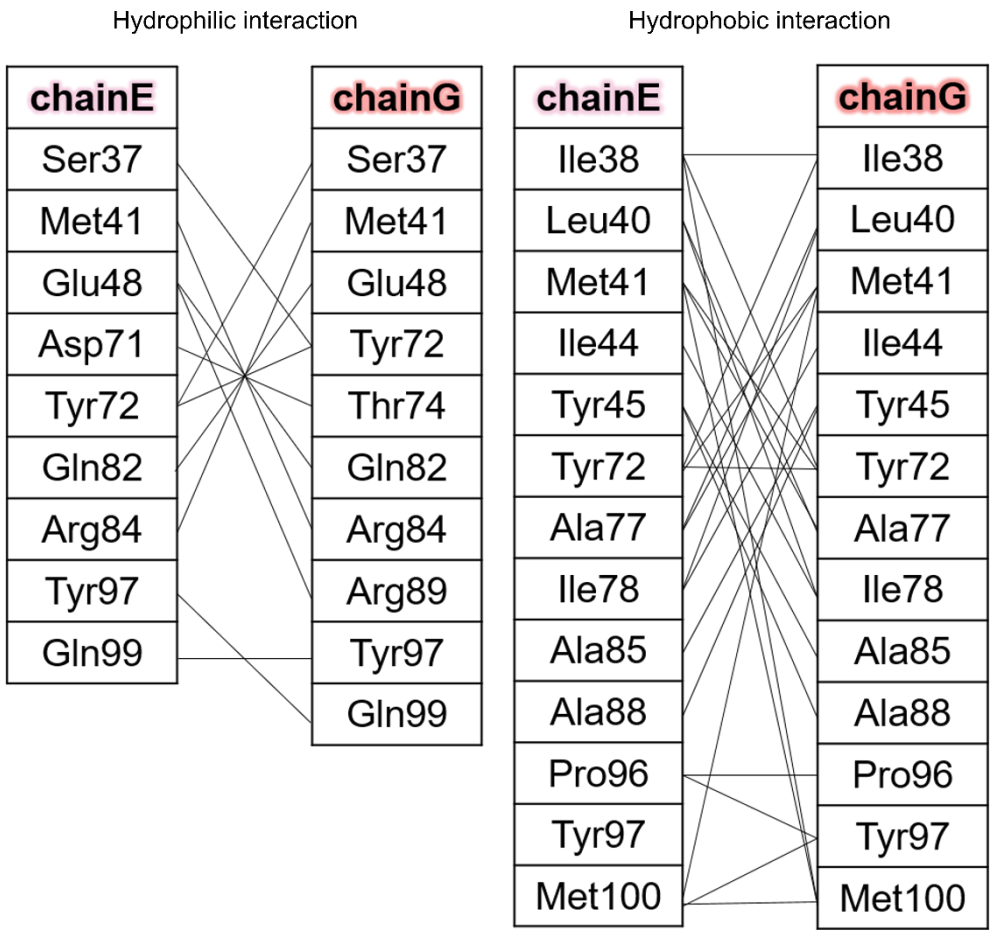

Figure 3. Schematic diagrams of the hydrophilic interactions (left) and hydrophobic interactions (right) contributed by the residues in the dimeric interface of $VapC_{LT2}$.

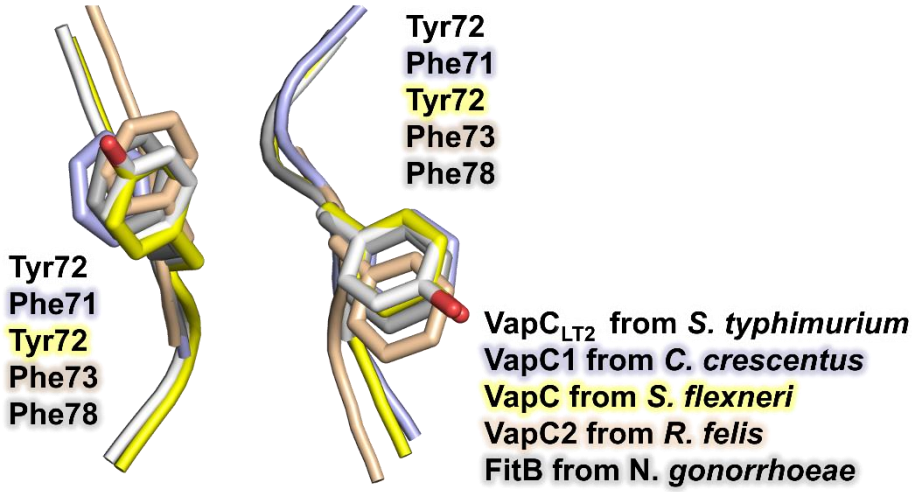

Figure 4. Superimposition of the conserved aromatic residues of VapC$_{LT2}$ and the homologs. C. *crescentus* VapC1 (purple), *S. flexneri* VapC (yellow), *R. felis* VapC2 and *N. gonorrhoeae* FitB (gray).

1.3.3 Identification of $VapC_{LT2}$ as a Ca^{2+}-dependent ribonuclease

$VapC_{LT2}$ contains a PIN domain that has metal-dependent nuclease activity. The PIN domain has four acidic residues that form a negatively charged cavity. The $VapC_{LT2}$ structure shows the active site in which four acidic residues, Asp7, Glu42, Asp98 and Glu119, form a negatively charged cavity to coordinate a metal ion (Figure 5A). The four acidic residues in the active site were stabilized via a hydrogen bonding network with neighboring residues such as Thr8, Asn9, and Thr10 (Figure 6A). These hydrogen bonding networks are also found in the homologs of $VapBC_{LT2}$. For instance, the conserved active site residue Asp4 of VapC15 from *M. tuberculosis* forms a hydrogen bonding network with its adjacent Thr5 and Ser6, and Asp4 and Ser6 of VapC30 from *M. tuberculosis* also form such a hydrogen bonding network (42,57).

VapC homologs from various organisms show Mg^{2+}- or Mn^{2+}-dependent nuclease activities. For example, VapC from *S. flexneri* cleaved MS2 RNA nonspecifically with Mg^{2+} or Mn^{2+} ions *in vitro* (9). However, $VapC_{LT2}$ showed no activity with either Mg^{2+} or Mn^{2+} *in*

vitro (9). We tried to find the putative coordinated metal of $VapC_{LT2}$ using a fluorescence quenching assay with fluorescence-labeled synthetic oligoribonucleotides (14 bases) as a substrate. This substrate was designed to contain AC nucleotides as a possible cleavage site, based on a previous study showing that $VapC_{LT2}$ specifically cleaves $tRNA^{fmet}$ between +38(A) and +39(C) *in vivo* (9). The effects of several divalent metal ions such as Ca^{2+}, Cd^{2+}, Co^{2+}, Mg^{2+}, Mn^{2+}, and Zn^{2+} were monitored. The results showed that the highest RNA substrate fluorescence was emitted in the presence of Ca^{2+}, indicating that this ion demonstrates the highest increase in the ribonuclease activity of $VapC_{LT2}$ (Figure 5B). $VapC_{LT2}$ without metal ions was significantly less active than $VapC_{LT2}$ with metal ions. Mg^{2+}, which is coordinated in the homologs from various organisms, shows lower activity than several other metal ions. Mn^{2+} and Co^{2+} ions show the second highest activity but weaker effects than that of Ca^{2+}. These fluorescence assay results are in agreement with ICP-MS data showing that the $VapC_{LT2}$ sample purified in the absence of any metal ions contains 18 μM Ca^{2+} ions per 100 μM $VapC_{LT2}$. It is

possible that the bound fraction of Ca^{2+} ions decreases due to the sample dilution for ICP-MS. We also tested the ribonuclease activity of 10 μM $VapC_{LT2}$ in the presence of increasing concentrations of Ca^{2+} ions (10 μM, 100 μM, 1 mM, 10 mM and 30 mM, Figure 5C). The strongest activity was observed in the presence of 1 mM Ca^{2+} ions. Higher concentrations of Ca^{2+} ions, which are not physiologically relevant, might deteriorate the structural integrity of the protein and RNA substrates. In the $VapBC_{LT2}$ structure, Ca^{2+} ions are positioned in a metal binding site whose amino acid positions are nearly identical to those of other VapC toxins (Figure 6B). Our crystallographic data, ICP-MS data, and fluorescence data strongly suggest that coordination of a Ca^{2+} ion to the active site function is an important factor in the ribonuclease activity of $VapC_{LT2}$. Interestingly, the Ca^{2+} dependence of VapC activity has not been reported until now. VapC homologs from various organisms primarily require Mg^{2+} or Mn^{2+} as a coordinated metal for nuclease activities; for instance, in the presence of Mg^{2+} or Mn^{2+} ions, VapC from *S. flexneri* nonspecifically cleaves MS2 RNA *in vitro* (9); VapC30 and

VapC26 from *M. tuberculosis* exhibit ribonuclease activity for a single-stranded RNA with randomly distributed bases (41,42); VapC5 from *M. tuberculosis* show ribonuclease activity for RNase alert kit substrate and 150 nucleotide sequence loop RNA (58); and VapBC15 from *M. tuberculosis* exhibits ribonuclease activity for total RNA of *E. coli* (57). Our results conclusively suggest that Ca^{2+} is a potential coordinated metal of $VapC_{LT2}$.

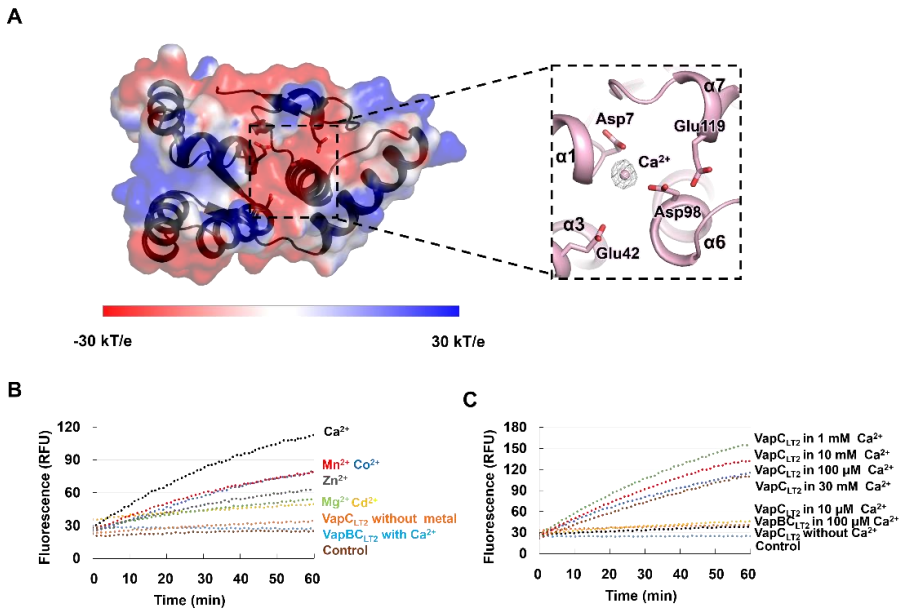

Figure 5. Active site structures of $VapC_{LT2}$ and ribonuclease assays of $VapC_{LT2}$ (**A**) The electrostatic surface potential of $VapC_{LT2}$ (chain E) is plotted at ±30 kT/e and also shown with the ribbon representation. The active site cavity is indicated by the black dotted rectangle. The electrostatic surface potential was calculated without the Ca^{2+} ion, and close-up views of the $VapC_{LT2}$ active site. The key residues shown in the stick models. Ca^{2+} is shown as the pink sphere (*mFo-Fc*; contoured at 2.5 σ). (**B**) Fluorescence quenching assay. *In vitro* ribonuclease assays were performed as described in the 'Materials and methods' section. For the assay, 10 μM $VapC_{LT2}$ (or $VapBC_{LT2}$), 100 μM metal ions and 40 units of RiboLock™ RNase inhibitor (Thermo Scientific) were included in a 50-μl reaction volume. Possible bound metal ions were removed before the assay using 30 mM EDTA. (**C**) For the assay, 10 μM $VapC_{LT2}$ (or $VapBC_{LT2}$) and 10 μM, 100 μM, 1 mM, 10 mM or 30 mM Ca^{2+} ions were included in a 50-μl reaction volume. Possible bound metal ions were removed before the assay using 30 mM EDTA. The control contained

100 μM Ca^{2+} ions and 40 units of RiboLock^{TM} RNase inhibitor (Thermo Scientific). Each experiment was performed in triplicate. Fluorescence was reported every 30 sec for 60 min.

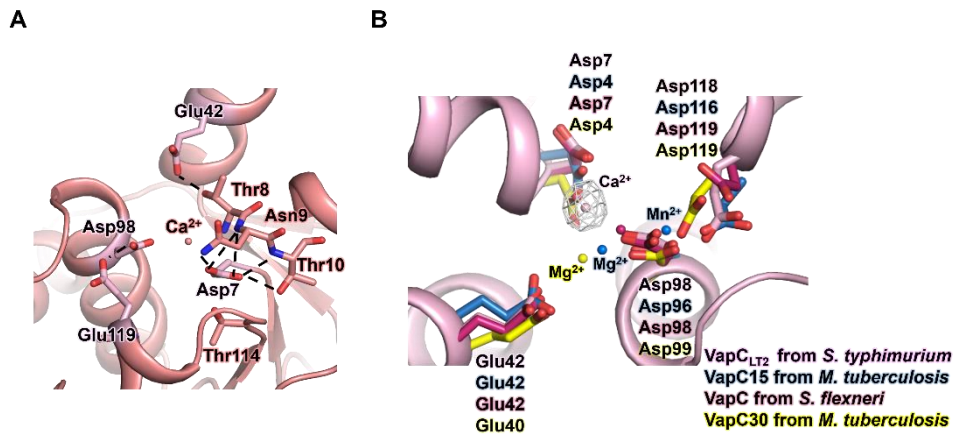

Figure 6. Active site structures of $VapC_{LT2}$ and homologs (A) Active site key residues of $VapC_{LT2}$ (pink), and the assistant residues (salmon). The hydrogen bonds and salt bridges are shown as the black dotted lines. Ca^{2+} is shown as the spheres. **(B)** Superposition of the key conserved residues of $VapC_{LT2}$ (pink), VapC15 (blue), and VapC30 (yellow) from *M. tuberculosis*, and VapC (purple) from *S. flexneri*. Each coordinated metal is shown as a sphere and labeled using the color of their components (*mFo−Fc*; contoured at 2.5 σ).

1.3.4 Interaction between $VapB_{LT2}$ and $VapC_{LT2}$

In the structure of the $VapBC_{LT2}$ complex, the C-terminal domain of the $VapB_{LT2}$ antitoxin binds to four α helices of $VapC_{LT2}$ (Figure 7A). The residues forming hydrophilic and hydrophobic interactions within the $VapBC_{LT2}$ interface are described in Figure 8. The α1 helix of $VapB_{LT2}$ binds to the α2 and α4 helices of $VapC_{LT2}$ via hydrophilic and hydrophobic interactions. Specifically, there are hydrophilic interactions between the $VapB_{LT2}$ α1 helix and $VapC_{LT2}$: interactions of (i) Pro42 on the α1 helix with Ser31 on the α2-α3 loop, (ii) Ser46 and Ser49 with Arg66 on the α4 helix, (iii) Asp48 with Arg23 and Asn27 on the α2 helix, (iv) Asp52 with Arg23 on the α2 helix, (v) Gly53 with Lys18 on the α2 helix, (vi) Glu54 with Arg55 on the α4 helix and Lys18 on the α2 helix, (vii) Gly55 and Ala56 with Arg55 on the α4 helix, and (viii) Ser57 with Asn56 on the α4 helix (Figure 7B). Additionally, there are hydrophobic interactions between the $VapB_{LT2}$ α1 helix and $VapC_{LT2}$: interactions of (i) Trp47 on the α1 helix with Phe26, Met33 on the α2 helix and Leu67 on the α4 helix, (ii) Trp50 on the α1 helix with Ile15 on the

α1 helix and Val59 and Phe63 on the α4 helix, and (iii) Phe51 on the α1 helix with Pro19, Ile22 and Phe26 on the α2 helix (Figure 7C). The hydrophobic interaction formed by these aromatic residues is highly similar to those observed in the VapBC complexes from *S. flexneri* and *R. felis* (50,55), which involve Trp47, Trp50 and Phe51 of *S. flexneri* VapB and Trp46 and Phe50 of *R. felis* VapB.

The interaction between $VapB_{LT2}$ and $VapC_{LT2}$ occurs elsewhere. The C-terminus loop of $VapB_{LT2}$ in the $VapBC_{LT2}$ complex binds to the α1, α3 and α6 helices of $VapC_{LT2}$ through hydrophilic and hydrophobic interactions: hydrophilic interactions of (i) Thr58 and Phe60 with Lys16 on the α1 helix, (ii) Asp59 with Leu51 on the α3-α4 loop, (iii) Arg64 with Glu42 on the α3 helix and Asp98 on the α6 helix, (iv) Glu65 with Tyr 45 on the α3 helix, and (v) Gln66 with Pro96, Tyr97 and Asp98 on the α6 helix (Figure 7D), and hydrophobic interactions of (i) Ala56 with Ile15 on the α1 helix, (ii) Phe60 with Leu43 and Ala47 on the α3 helix and Ile12, Ile15 on the α1 helix, (iii) Met61 with Ile12 on the α1 helix, and (iv) Pro67 with Pro96 and Tyr97 on the α6 helix (Figure 7E).

Notably, Arg64 and Gln66 on the C-terminal loop of $VapB_{LT2}$ interact with Glu42, Asp98 and Glu119 on $VapC_{LT2}$, which are conserved residues associated with toxin activity, and the interactions with conserved residues are predicted to have a significant inhibitory effect on toxin activity (Figure 9A). Similar interactions between the arginine residue on the C-terminal loop of $VapB_{LT2}$ and the $VapC_{LT2}$ active site are observed in homologs of $VapBC_{LT2}$. For instance, in *S. flexneri* VapBC, Arg64 and Gln66 of VapB interact with Asp98 and Glu42 in the active site of VapC (49); in *C. crescentus* VapBC1, Arg68 of VapB1 interacts with Glu40 and Asp95 in the active site of one protomer of the VapC1 dimer, and Arg76 of VapB1 interacts with the same residues in the other protomer (51); in *R. felis* VapBC2, Arg66 of VapB2 interacts with Glu43 and Asp99 in the active site of one protomer of the VapC2 dimer, and Arg74 of VapB2 interacts with the same residues of the other protomer (50); in *M. tuberculosis* VapBC15, Arg74 of VapB15 interacts with Glu42 in the active site of one protomer of the VapC15 dimer (53); and in *M. tuberculosis* VapBC3, Arg73 of VapB3 interacts

with D117 and D119 in the active site of one protomer of VapC3 (59) (Figure. 8B). In other words, $VapBC_{LT2}$ and VapBC from *S. flexneri* (the closest homolog of $VapBC_{LT2}$), and their single VapB antitoxin bind to the cognate toxin alone, but the other single VapB antitoxins from various organisms interacts with the toxin dimer (Figure 9B). Additionally, bioinformatics analysis showed the common existence of palindromic sequences at the C-terminal of the VapC binding region of VapB, and a difference in the palindromic pattern might have caused the diversity in the VapBC interaction (51). The palindromic sequence of $VapB_{LT2}$ can be characterized as "R64E65Q66 ... Q70E71R72". Although the binding ratio between VapB and VapC is different, VapB inhibits the activity of VapC and the C-terminal of VapB interacts with the active site residues of VapC; still, it remains to be elucidated how the differences in binding modes of VapB affect its inhibitory effect on the activity of VapC.

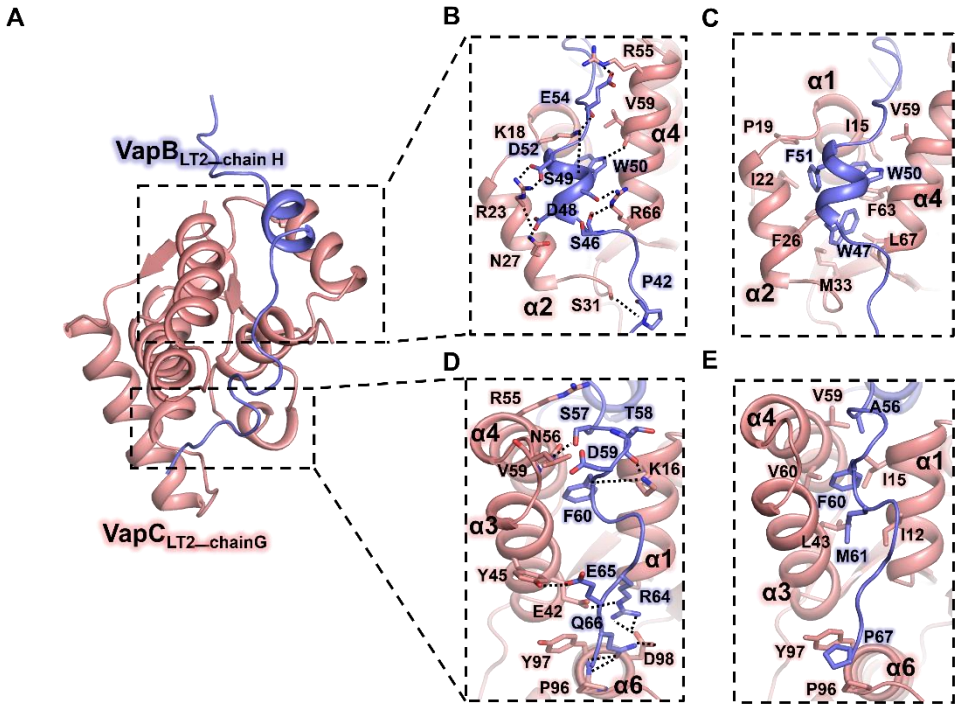

Figure 7. Interaction between $VapB_{LT2}$ and $VapC_{LT2}$ (A) The region of interaction is indicated by the black dotted rectangles. (B and C) The residues involved in the hydrophilic and hydrophobic interactions between the α1 helix of $VapB_{LT2}$ and the $VapC_{LT2}$ toxin. The hydrogen bonds and salt bridges are shown as the black dotted lines, and the residues participating in the interactions are shown in the stick models. (D and E) The residues involved in the hydrophilic and hydrophobic interactions between the C-terminal of $VapB_{LT2}$ and the $VapC_{LT2}$ toxin. The hydrogen bonds and salt bridges are shown as the black dotted lines, and the residues participating in the interactions are shown in the stick models.

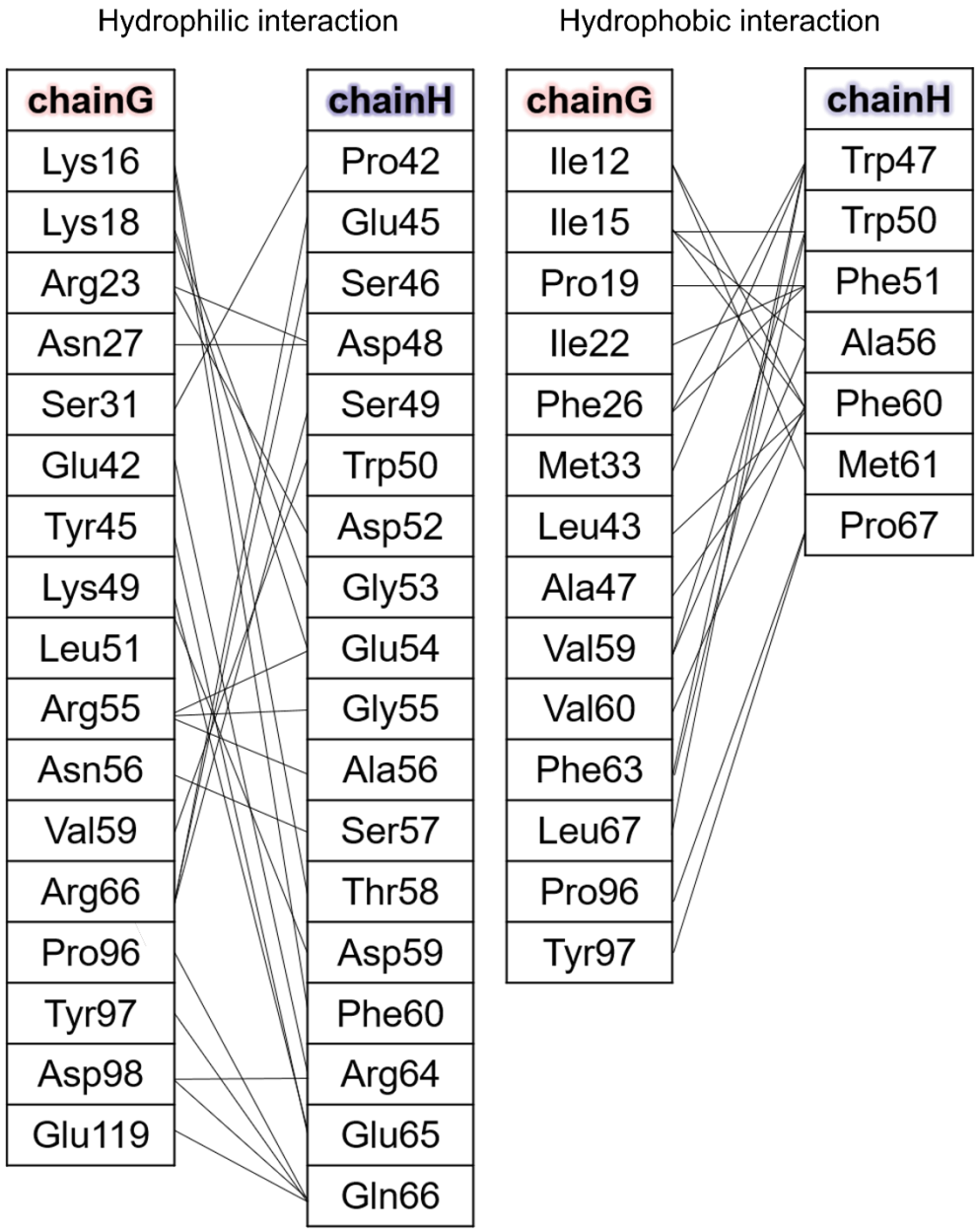

Figure 8. Schematic diagrams of the hydrophilic interactions (left) and hydrophobic interactions (right) contributed by the residues in the interaction interface of $VapBC_{LT2}$.

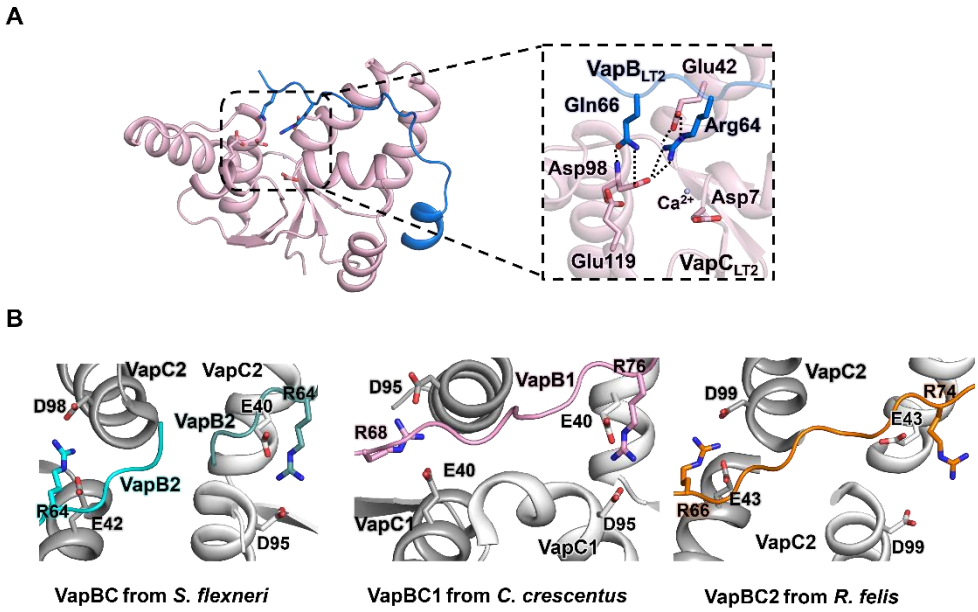

Figure 9. Interaction between VapB and VapC, as mediated by the arginine residue on the C-terminal of VapB (A) Inhibitory interactions between $VapB_{LT2}$ and $VapC_{LT2}$. Close-up views of the interactions at the active sites of $VapC_{LT2}$. The key residues of $VapC_{LT2}$ are shown as the light pink sticks, and the interacting residues of $VapB_{LT2}$as the blue sticks. Ca^{2+} is shown as the spheres. The hydrogen bonds and salt bridges are shown as the black dotted lines. (B) Interactions between VapB and VapC, as mediated by the arginine residue on the C-terminal of VapB of the $VapBC_{LT2}$ homologs. The key residues of the VapCs are shown in the white and gray stick models, and the arginine residues of the VapBs as the cyan (*S. flexneri* VapB), pink (*C. crescentus* VapB1) and orange (*R. felis* VapB2) stick models.

1.3.5 Overall structure of $VapBC_{LT2}$ bound to DNA

We also determined the structure of $VapBC_{LT2}$ bound to a 27 bp double-stranded DNA to a resolution of 2.8 Å by molecular replacement using the structure of the DNA-free $VapBC_{LT2}$ complex as a search model, and the empty part of $VapB_{LT2}$ was filled by adjusting the map and sequence. The space group of the $VapBC_{LT2}$ bound to the DNA structure was $P3_1$, and there were four $VapBC_{LT2}$ in the asymmetric unit (Figure 10A). The complex structure includes 528 amino acid residues for $VapC_{LT2}$ (residues 1-132 for chain A, B, C and D), 272 amino acid residues for $VapB_{LT2}$ (residues 1-68 for chains E, F, G and H) and 149 water molecules in the crystallographic asymmetric unit. The structures of the DNA-free (described above) and DNA-bound forms of $VapBC_{LT2}$ superimpose well, suggesting that the conformation of the $VapBC_{LT2}$ interaction is not affected by DNA binding. In the structure of the DNA-bound form, we observed the N-terminal DNA-binding domain of $VapB_{LT2}$ which was not observed in the DNA-free form (Figure 10A). As seen in the side view of the DNA-bound form, the N-terminal domains of $VapB_{LT2}$

form a homodimer to bind to the major groove of DNA, and the C-terminal region of each monomer in the $VapB_{LT2}$ dimer binds to the cognate subunit in the $VapC_{LT2}$ homodimer, resulting in a heterotetrameric $VapBC_{LT2}$ complex with a stoichiometry of 2:2. The bound DNA adopts a B DNA-like conformation in a linear form with a major groove 25 Å in width and a minor groove 12 Å in width, which are obviously different from the bent DNA bound to the VapBC complexes from *C. crescentus* and *R. felis* (Figure 11). Similar to the structure of DNA-bound $VapBC_{LT2,}$ the structure of the FitAB-DNA complex from *N. gonorrhoeae* shows a linear DNA conformation with 36 base pairs and FitB is also one of the homologs of $VapC_{LT2}$ (Figure 12). However, the overall conformation of DNA-bound FitAB differs from that of DNA-bound $VapBC_{LT2}$ because the DNA-binding motif of FitA is an RHH motif, in contrast to the DNA-binding motif of $VapB_{LT2}$ (56).

Notably, the DNA-bound $VapBC_{LT2}$ structure revealed new $VapC_{LT2}$ dimer-dimer contacts between four $VapC_{LT2}$ proteins in DNA-bound $VapBC_{LT2}$ complexes that simultaneously bind to one

DNA molecule (Figure 10B), which was not observed between two $VapC_{LT2}$ dimers in the structure of the DNA-free VapBC complex. The interactions may stabilize the DNA-bound $VapBC_{LT2}$ complex, accelerating the binding of the $VapBC_{LT2}$ complex to the corresponding promoter DNA. The toxin dimer-dimer contacts in the DNA-bound form were calculated by *PISA*; in the DNA-bound VapBC complex from *R. felis*, two residues contribute, and in the DNA-bound VapBC complex from *C. crescentus*, seven residues are involved. In the DNA-bound $VapBC_{LT2}$, 18 residues are involved in the $VapC_{LT2}$ toxin dimer-dimer contacts. In addition, the diameter between the homologs was measured by PyMOL which showed that $VapBC_{LT2}$ binds more compactly, even though the DNA bound to VapBC1 from *C. crescentus* and VapBC2 from *R. felis* have the same number of base pairs (Figure 12). The residues involved in the hydrophilic interaction and hydrophobic interaction between the four $VapBC_{LT2}$ complexes are provided in Figure 13.

The expression of the TA complex is regulated through the interaction of the DNA-binding motif in the antitoxin with the

palindromic sequence in the promoter region of the TA operon (60). We conducted a fluorescence polarization assay to measure the binding affinities of each of the two palindromic DNAs (DNA I and II) present in the promoter region of $VapBC_{LT2}$. The measured dissociation constant (Kd) of the $VapBC_{LT2}$ complex with each of two palindromic sequences were 2.8 ± 0.6 μM (DNA I) and 1.87 ± 0.4 μM (DNA II) (Figure 14). DNA I bound to the $VapBC_{LT2}$ complex was successfully crystallized despite the dissociation constant between DNA I and $VapBC_{LT2}$ being relatively larger than that between DNA II and $VapBC_{LT2}$.

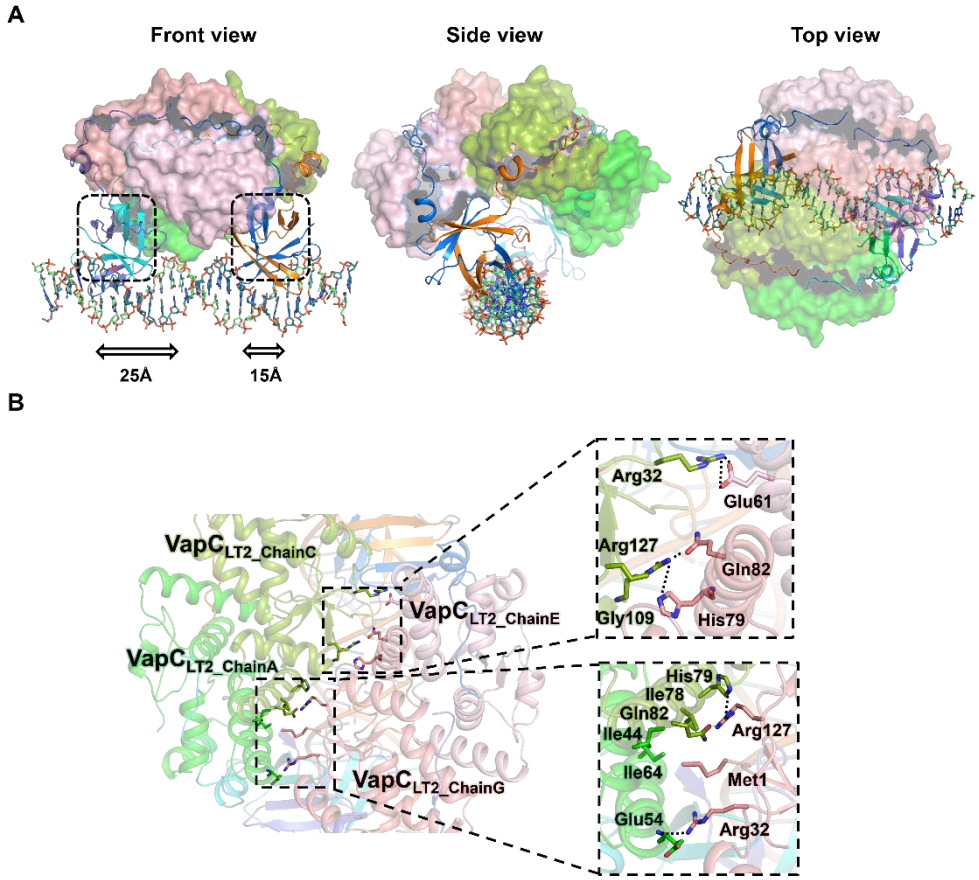

Figure 10. Structure of the DNA-bound VapBC$_{LT2}$. (A) Three viewpoints of the DNA-bound VapBC$_{LT2}$. The VapC$_{LT2}$ toxin is shown as the surface representation, and each VapC$_{LT2}$ toxin is expressed by a different color of their chain. VapB$_{LT2}$ are shown as the ribbon representation. DNA is shown in the stick model. In the front view, each of two-way arrows indicate the widths of the major grooves and minor grooves. The DNA groove lengths are measured by PISA. The N-terminal of VapB$_{LT2}$, which is disordered in the DNA-free VapBC$_{LT2}$, is indicated by the black dotted rectangle. (B) Interaction between the two VapC$_{LT2}$ dimers. VapC$_{LT2}$ is shown as the semi-transparent surface representation. The residues making contacts are shown in the stick model. Each VapC$_{LT2}$ residue is labeled using the colors of their components. The hydrogen bonds and salt bridges are shown as the black dotted lines.

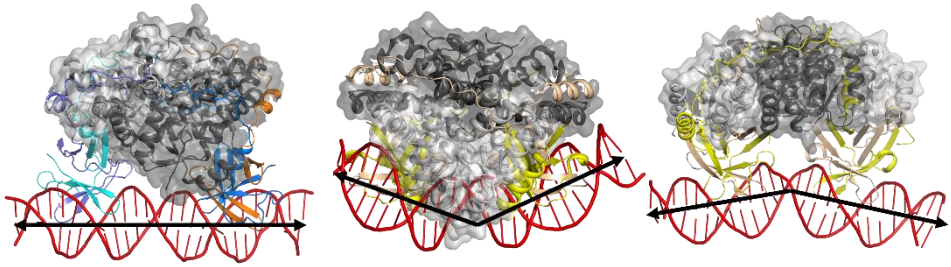

Figure 11. Comparison of DNA shape in DNA-bound VapBC. DNA shown on cartoon model (red). VapB antitoxin are shown as ribbon representation. VapC toxin are shown in semi-transparent surface representation.

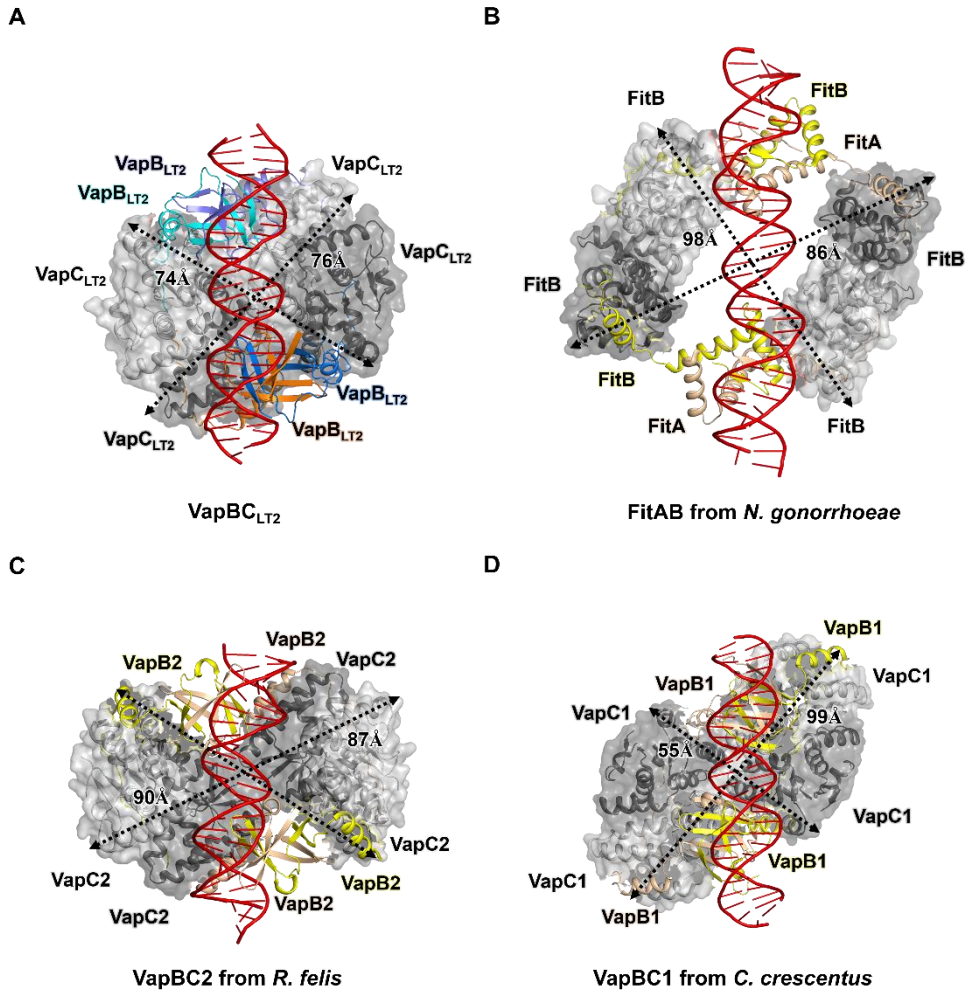

Figure 12. Overall structure of the DNA-bound VapBC complex from *S. eneterica* Typhimurium LT2 and homologs (A) DNA-bound VapBC$_{LT2.}$ (B) DNA-bound FitAB from *N. gonorroheae.* (C) DNA-bound VapBC2 from *R. felis.* (D) DNA-bound VapBC1 from *C. crescentus.* DNA is shown as a ribbon representation (red). The VapB antitoxin is shown as the ribbon representation. The VapC toxin is shown as the semi-transparent surface representation. Each diameter was measured by PyMOL.

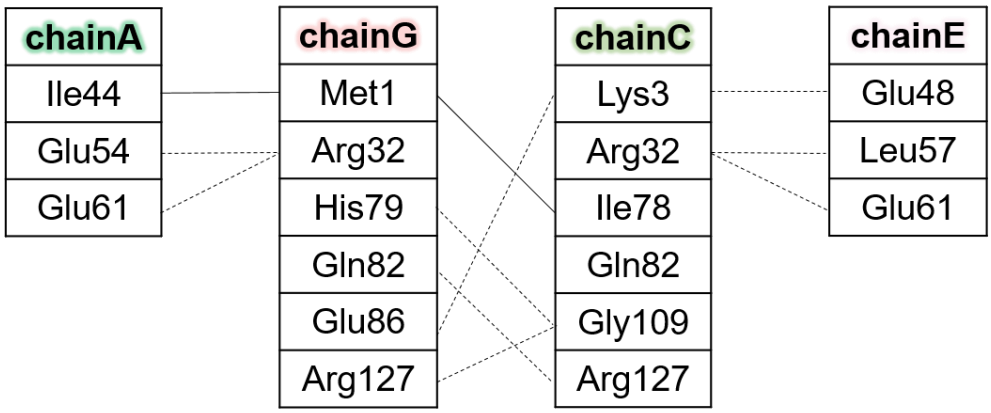

Figure 13. Schematic diagrams of the hydrophilic and hydrophobic interactions contributed by the residues in the two $VapC_{LT2}$ dimers of the DNA-bound $VapBC_{LT2}$ structure. The hydrogen bonds and salt bridges are shown as the black dotted lines. The hydrophobic interactions are shown as the black lines.

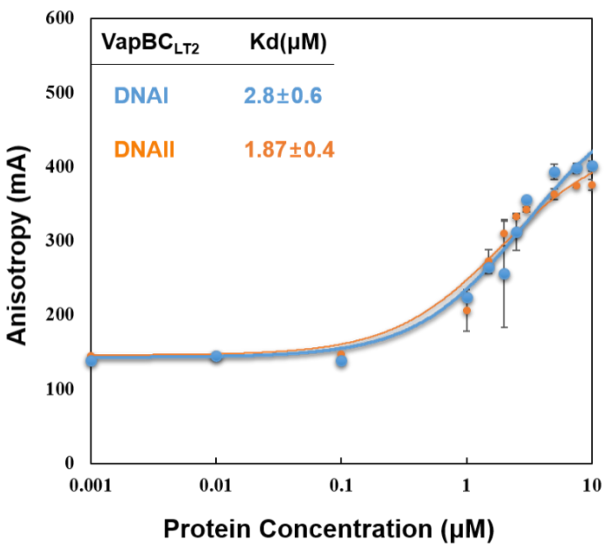

Figure 14. Fluorescence polarization assays for the DNA-binding affinities. The $VapBC_{LT2}$ binding assay was performed with its own promoter site. The plots of DNA I and DNA II are shown in blue and orange, respectively. The average values of the triplicate measurements and standard deviations are shown.

1.3.6 DNA-binding mode of $VapB_{LT2}$

The structures of the antitoxins in the asymmetric unit are almost identical. The structure of $VapB_{LT2}$ could be divided into two parts based on their roles: the N-terminal AbrB-type domain binds to DNA, and the C-terminal region binds to $VapC_{LT2}$ toxin (Figure 15A). Each of $VapB_{LT2}$ monomers contains four β-strands and one α helix. The N-terminal β-strands of each $VapB_{LT2}$ antitoxin form a β-sheet with those of the other antitoxin, resulting in a homodimer of the N-terminal domains of $VapB_{LT2}$. Specifically, the dimerization is mediated by the $\beta 2-\beta 2$ strand interaction and the $\beta 4-\beta 4$ strand interaction, and partially by the $\beta 1-\beta 3$ strand interaction (Figure 15B). The N-terminal β-sheets are located in the major groove of DNA. The midmost portion of the $VapB_{LT2}$ antitoxin structure is the hinge region, which may act as a flexible junction between DNA and the toxin-binding domains. The residues involved in the hydrophilic and hydrophobic interactions that form the $VapB_{LT2}$ dimer are shown in Figure 16.

There are five major residues, Ser8, Asn9, Arg10, Arg15, and

Lys18, on the N-terminal β strands of $VapB_{LT2}$ that interact with the DNA base or backbone phosphate (Figure 15C). There are paired interactions between chain BH of the $VapB_{LT2}$ dimer and the DNA: (i) Ser8 on chain B interacts with the nucleotide A19 base via hydrogen bond, and Arg15 on chain H interacts with the nucleotide A19 phosphate backbone (Figure 17A); (ii) Arg10 on chain B and Lys18 on chain H interact with the backbone phosphate of the nucleotide G16 (Figure 17B); (iii) Ser8 on chain H interacts with the nucleotide T5 base via hydrogen bonding, and Arg15 on chain B interacts with the phosphate backbone of nucleotide T5; (iv) Arg10 on chain H and Lys18 on chain B interact with the backbone phosphate of nucleotide T2. This paired-interaction was also observed in the chain DF dimer, but the interaction of Ser8 and Arg10 of chain D with DNA was difficult to observe due to the poor electron density maps of the β1 strand on chain D of $VapB_{LT2}$ (Figure 18). The side-chain nitrogen of Asn9 on Chain D interacts with nucleotides G4 and T5. The side-chain oxygen of Asn9 on Chain F interacts with nucleotides A17 and C10, and its side-chain nitrogen interacts with T9 (Figure 17C). Two

DNA-binding conformers of the Asn9 side-chain are also observed. The residue-specific interaction of $VapBC_{LT2}$ with DNA is shown in Figure 19.

We also searched for similar DNA-binding residues in three homologs whose structures are already known. The side-chain oxygen of Ser14 of one protomer and the main-chain nitrogen of Arg21 of the other protomer in VapB1 from *C. crescentus* interact with the base and phosphate backbones of nucleotide G6, respectively. The side-chain oxygen and main-chain nitrogen of Asn13 of VapB1 interact with nucleotides A16 and T17 respectively. (51). The side-chain oxygen of Ser12 of one protomer and the main-chain nitrogen of Lys19 of the other protomer in the VapB2 dimer from *R. felis* interact with phosphate backbone of nucleotide A2. In the DNA-bound FitAB complex from *N. gonorrhoeae*, the side chain nitrogen of Arg7 of one protomer and the side-chain oxygen of Thr28 and Glu29 of the other protomer in FitA interact with the base and backbone phosphates of nucleotide G6, respectively. The Asn8 shows a water-mediated interaction with DNA, unlike Asn9 of

$VapB_{LT2}$ (56).

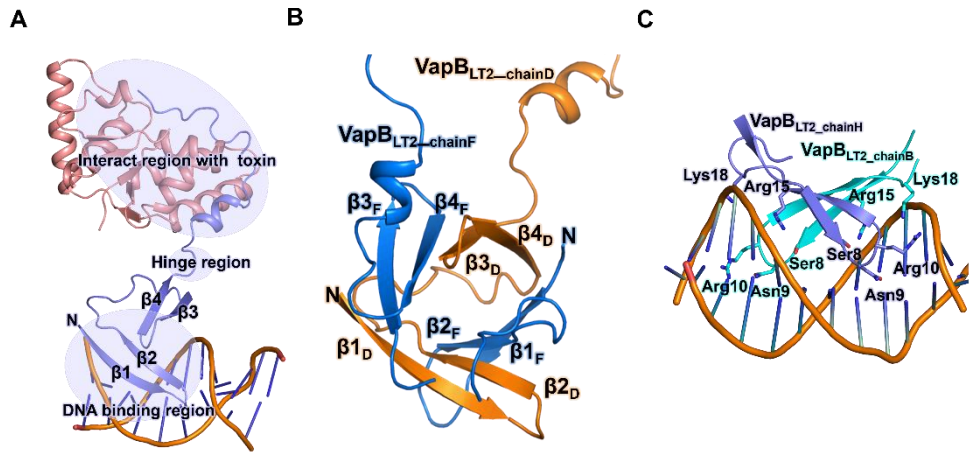

Figure 15. Structure of the DNA-bound VapB$_{LT2}$ antitoxin. (A) The three parts are divided based on the roles of the antitoxin. The top circle part is the interaction with the VapC$_{LT2}$ toxin. The middle circle is the hinge region, and the lower circle is the interaction region with DNA. VapBC$_{LT2}$ and DNA are shown in the ribbon representation. (B) VapB$_{LT2}$ antitoxin dimer. (C) Details of the interaction residues of the VapB$_{LT2}$ dimer made by monomers B and H with DNA. The VapB$_{LT2}$ residues are labeled in the colors of their components. DNA is shown in the ribbon representation.

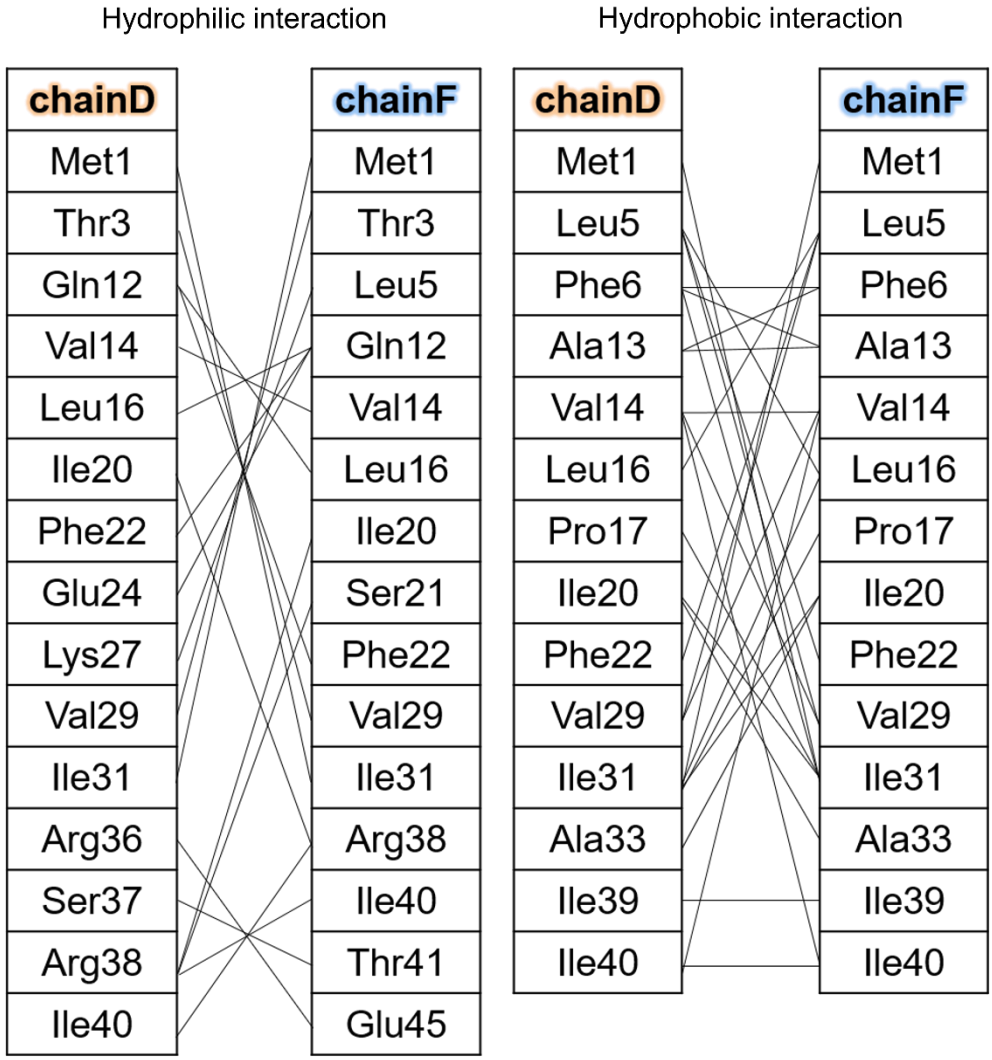

Figure 16. Schematic diagrams of the hydrophilic interactions (left) and hydrophobic interactions (right) contributed by the residues in the interaction of the $VapB_{LT2}$ dimer of the DNA-bound $VapBC_{LT2}$ structure.

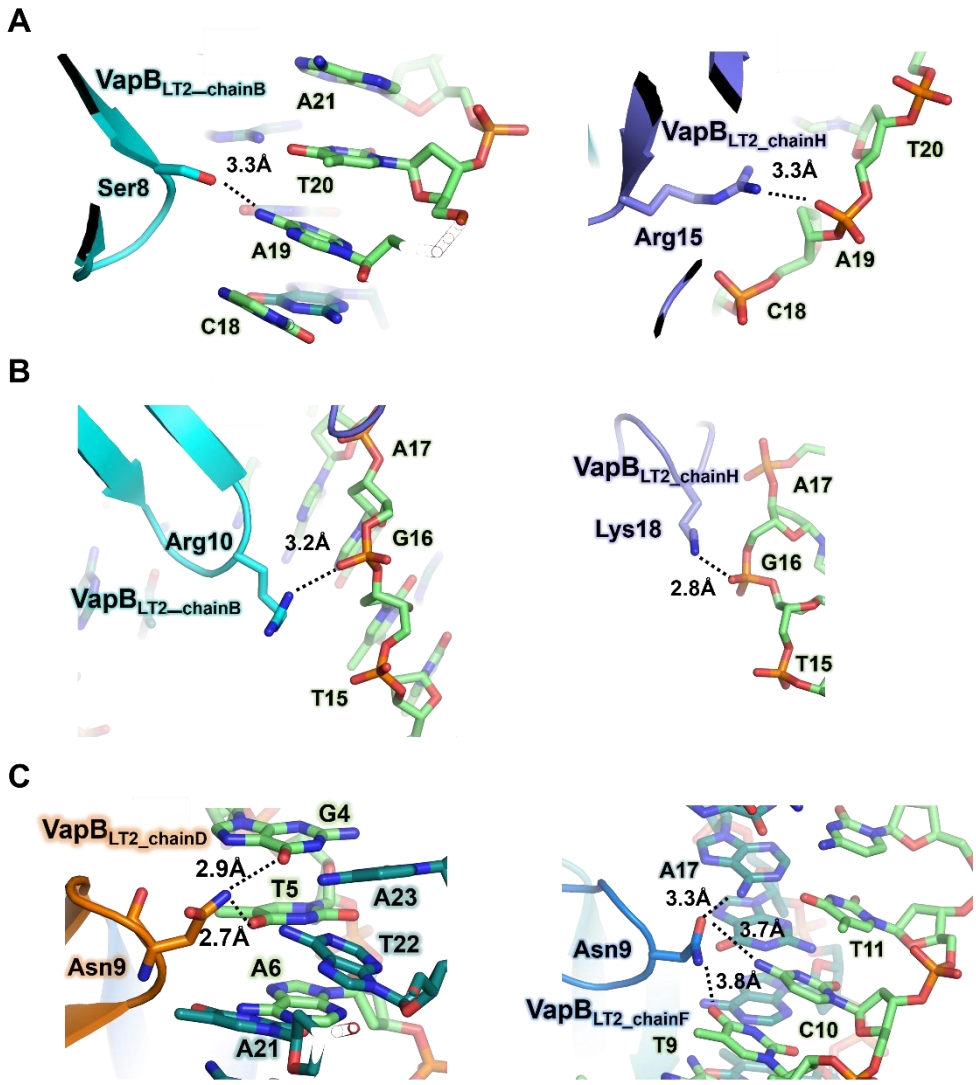

Figure 17. Detailed interactions between VapB$_{LT2}$ and DNA (A) Left: Interaction of VapB$_{LT2}$ Ser8 on chain B with the nucleotide A19 base. Right: Interaction of VapB$_{LT2}$ Arg15 on chain H with the nucleotide A19 backbone phosphate. **(B)** Left: Interaction of VapB$_{LT2}$ Arg10 on chain B with the nucleotide G16 backbone phosphate. Right: Interaction of VapB$_{LT2}$ Lys18 on chain H with the nucleotide G16 backbone phosphate. **(C)** Left: Interactions of Asn9 on chain D with G4 and T5 of DNA. Right: Interactions of Asn9 on chain F with T9, C10 and A17. Each interaction is shown as a dotted line.

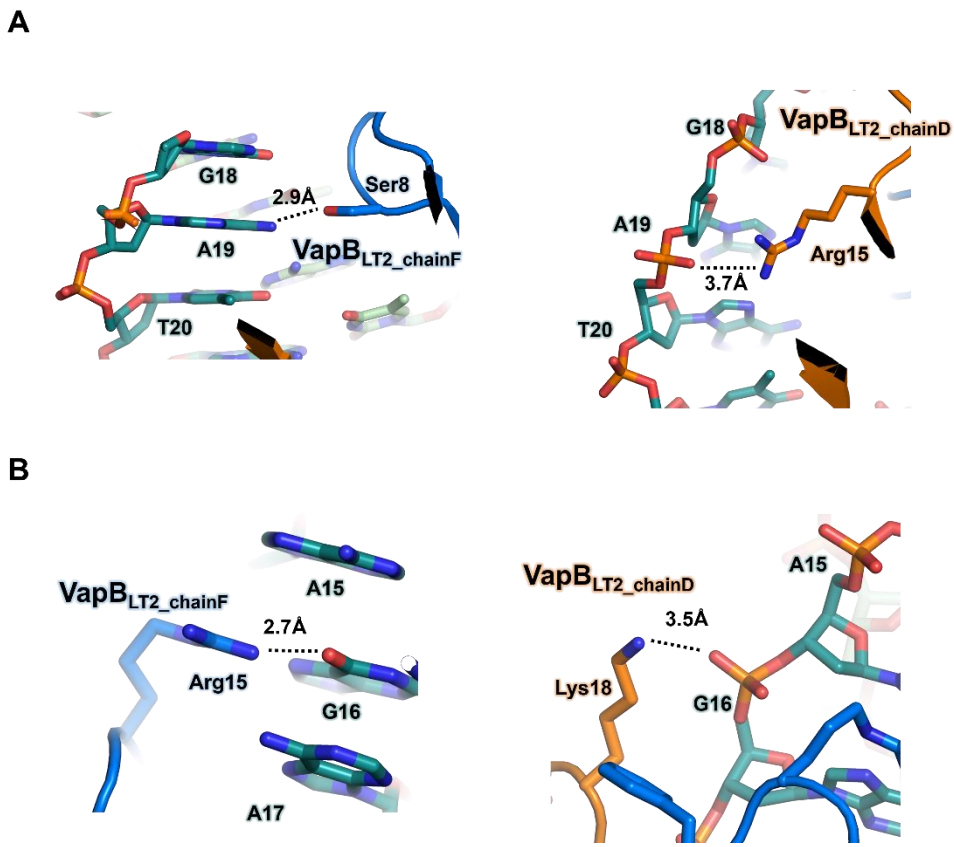

Figure 18. Detailed interactions between the VapB$_{LT2}$ antitoxin and DNA (A) Left: Interaction of Ser8 on chain F with the nucleotide A19 base. Right: Interaction of Arg15 on chain D with the nucleotide A19 backbone phosphate. (B) Left: Interaction of Arg10 on chain F with the nucleotide G16 bases. Right: Interaction of Lys18 on chain D with the nucleotide G16 backbone phosphate.

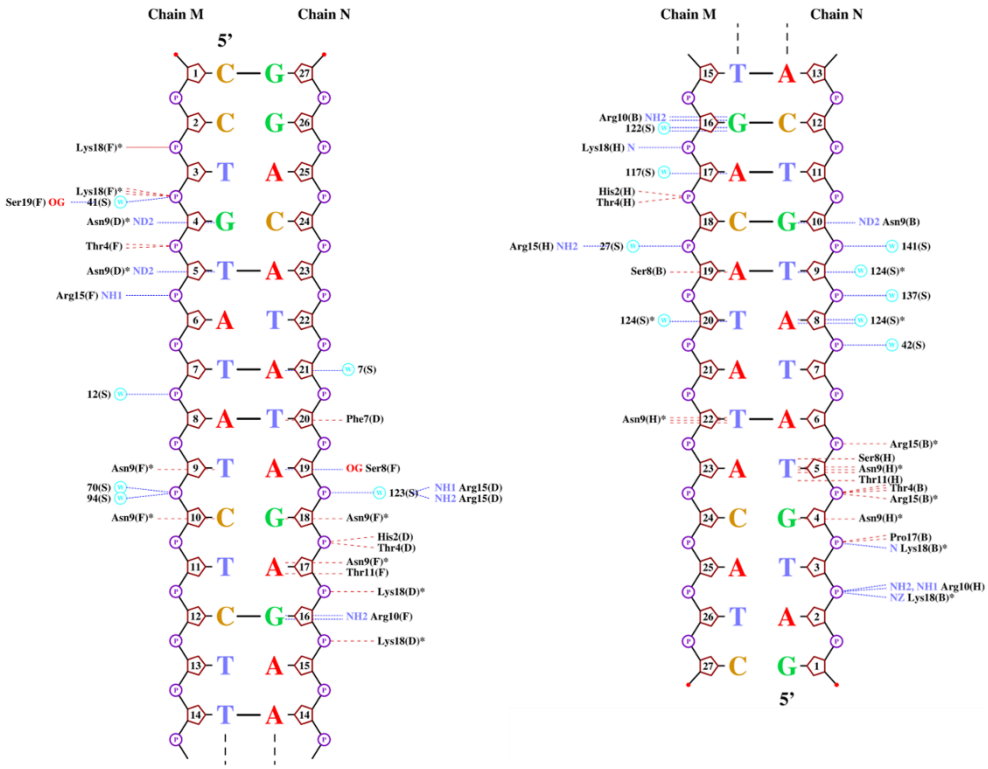

Figure 19. Analysis of the contacts between the $VapB_{LT2}$ antitoxin and DNA. The hydrogen bonds and non-bonded contacts are represented as the dashed blue and red lines, respectively. The interaction between the protein and DNA model was visualized using NUCPLOT (56).

1.4 Conclusion

A recent study showed that at least 14 type II TA systems are present in *S.* Typhimurium LT2 (11). Additionally, a few studies have demonstrated the physiology of VapBC from *S.* Typhimurium LT2 (8-10). However, their structural information is not available currently. In this study, we determined the DNA-free and DNA-bound structures of the $VapBC_{LT2}$ complex. In addition, we identified the $VapC_{LT2}$ toxin as a Ca^{2+}-dependent ribonuclease, which was consistent with our crystal structure of the $VapC_{LT2}$ active site bound to Ca^{2+}. In contrast, previous studies have shown that VapC toxins from many organisms use Mg^{2+} or Mn^{2+} ions to function as a ribonuclease. Combining the only currently available structures of DNA-bound VapBC complexes from *C. crescentus* and *R. felis*, our structural studies could contribute to an understanding of a mode of interaction between the VapBC family and the corresponding promoter DNA. Two approaches are to develop antibiotic peptides that mimic the $\alpha 1$ helix of $VapB_{LT2}$ or the $\alpha 2$ and $\alpha 4$ helixes of

$VapC_{LT2}$. $VapB_{LT2}$-mimicking peptides should be considered if they do not interfere with either the active site and the substrate-binding site of $VapC_{LT2}$. $VapC_{LT2}$-mimicking peptides compete with $VapC_{LT2}$ to bind $VapB_{LT2}$. Similar approaches have been employed; for instance, previous structural studies on *M. tuberculosis* VapBC have aided the design of synthetic peptides to disrupt the VapBC interaction and thus increase the amount of free VapC toxins, which produce antibiotic effects (41,42). Based on the structure of the $VapBC_{LT2}$-DNA complex, antibiotic peptides that mimic the DNA-binding region of $VapB_{LT2}$ could be designed to bind to the promoter DNA of the VapBC operon, leading to its transcriptional repression and elevating the level of free VapC toxins in cells.

Chapter 2. Crystal structure of the novel toxin-antitoxin complex SehAB from *Salmonella* Typhimurium LT2: implication into pathogenicity with its unique interaction mode

2.1. Introduction

The salmonella bacteria belongs to the Enterobacteriaceae family, which are rod-shaped, Gram-negative, and facultative anaerobic pathogens (61,62). These pathogens have infected over 21.7 million people globally and are responsible for 200,000 deaths on an annual basis primarily due to poor sanitary conditions (63). Salmonellae infections can also affect animals through contaminated food or water, which can ultimately lead to serious cross-contamination to humans (64). Upon infection, the symptoms ranges from mild gastroenteritis to severe systemic diseases such as typhoid-fever, septic shock, and hypovolemic shock (65). The salmonellae are divided into two species, *Salmonella bongori* and *Salmonella enterica*. The pathogenic

S. enterica, is further classified into six subspecies that includes two representative bacterial pathogens, *S.* Typhi and *S.* Typhimurium (65). Because the tissues observed in *S.* Typhimurium-infected are similarly distributed in typhoid fever patients, murine typhoid has been used as an animal model for the study of typhoid fever (66). Interestingly, a number of toxin-antitoxin (TA) modules exist in the pathogenic *S. enterica* whereas non-pathogenic *S. bongori* was reported to have no TA modules (67). Because TA modules are known to be closely related to pathogenicity of bacterial pathogens, structural and functional study on the TA modules from Salmonella species can lead to a rational, anti-Salmonellae infections approach. The other representative instance is the TA modules observed in *Mycobacteria tuberculosis*. Until now, over 88 TA modules have been identified and active researches have been performed in the pathogenic *M. tuberculosis* (68,69), while no structural TA module information from Salmonella species have been reported. Bacteria contain toxin-antitoxin (TA) pairs which were previously known as addiction modules (70,71). The TA pairs are generally classified into

six types– based on the genetic structure and regulation modes of antitoxin molecules (20,21). In types I and III TA systems, the antitoxins are RNA molecules which directly inhibit translation or regulate activities of toxins. Specifically, in type I TA system, antitoxins directly bind to mRNA molecules of toxins as unstable antisense RNAs, while antitoxins of sRNA in the type III TA system bind to toxin and neutralize the activities of the toxins. The TA systems of type IV and type V were recently reported (24) . In both type IV and type V TA systems, the antitoxins function as proteins. In type IV TA system, antitoxins bind to target proteins of type IV toxins to stabilize the target proteins, leading to suppression of the activities of toxins (26). In type V TA system, antitoxins degrade mRNA of toxins and inhibit translation of type V toxins (24). In type VI TA system, the type VI toxin SocB is unstable and degraded by the protease ClpXP, but toxin degraded by ClpXP needs the proteolytic adaptor antitoxin SocA (25). In type II TA system, TA pairs are composed of stable toxin molecules and labile antitoxin molecules. Under normal conditions, specific activities of toxin

molecules are inhibited by antitoxin molecules as they form a rigid complex. However, under stressful environments accompanying oxidative stress, temperature changes, starvation caused by malnutrition, and treatment of antibiotics, different kinds of proteases produced by host cells degrade the antitoxin molecules. As a result, death or growth inhibition of host cells are observed (28,29). Recently, novel type II TA module (SehAB) of *S.* Typhimurium was reported to promote virulence in mice (67). From the study, the bacteria expressing active SehAB proteins were reported to be predominantly localized in the mesenteric lymph nodes (67). In addition, SehAB was essential for the survival of Salmonella in these peripheral lymphoid organs, which is important in understanding pathogenicity of Salmonellae (67). Despite importance of SehAB, structural and functional studies on SehAB from *S.* Typhimurium remains unknown. Here, we report the first TA module crystal structure of SehAB complex from *S.* Typhimurium 2.49 Å. In the crystal structure, two TA complexes interact with each other via N-terminal antitoxin-interacting domain in the antitoxin protein,

resembling a horseshoe in overall oligomeric shape. Many kinds of antibiotics have been developed and used to eradicate bacterial pathogens. However, bacterial pathogens develop resistance to antimicrobial drugs and thus many antibiotics are losing their potency. Therefore, there is an urgent need for the discovery of new antibacterial targets and development of novel antibiotics. Our structural and functional study may accelerate the development of novel and site-specific antibiotics that can be used to effectively eradicate *S.* Typhimurium.

2.2. Materials and Methods

2.2.1. Gene cloning

The SehB (STM4030) and SehA (STM 4031) genes from *S.* Typhimurium LT2 were amplified by polymerase chain reaction (PCR) using the genomic DNA from *S.* Typhimurium LT2 as a template (72). The forward and reverse primers were 5' -GCG GT CAT ATG AGA ACT CAT CGT CAG ATG GAT G-3' /5' -GAT TA CCG CTC GAG

TTA CTC GAT GAA GGC ATC TGC T-3' for SehB (STM 4030), and 5'-GAT TA CAT ATG CAT GTT ATC AGC CGA AAA CCG -3' /5' - GCG GT CCG CTC GAG TTA TTT ATT ACC CCG ATA GTA TG-3' for SehA (STM 4031), respectively. The restriction enzymes sites of *Nde*I and *Xho*I used for cloning are underlined. The genes of SehB (STM4030) and SehA (STM 4031) were cloned into the expression vectors pET-21a(+) (Novagen) and pET-28a(+) (Novagen), respectively. The construct of SehB has no tag added to the recombinant protein, while that of SehA has twelve-residue tag (MGSSHHHHHHSSGLVPRGSH) added to the amino terminus of the recombinant protein. The sequences of both SehA and SehB were confirmed by DNA sequencing. The SehA (STM 4031) truncated genes (Met1-Ser87, Met1-Ala89, Met1-Asp92) from *S.* Typhimurium LT2 were amplified by polymerase chain reaction (PCR) using the genomic DNA from *S.* Typhimurium LT2 as a template (72). The reverse primers were 5' - GCG GTC CGC CG CTCG AG TTA GGA AAC GAT ATG TTT CAC AAA TAT C-3' for SehA truncated gene Met1-Ser87, 5' - GCG GTC CGC CG CTC GAG TTA GGC

ATG GGA AAC GAT ATG TTT CAC-3' for SehA truncated gene Met1-Ala89 and 5' - GCG GTC CGC CG CTC GAG TTA GTC ATA TTC GGC ATG GGA AAC GA -3' for SehA truncated gene Met1-Asp92 respectively. The restriction enzyme site of *Xho*I used for cloning is underlined. The SehA with thioredoxin tag gene from *S.* Typhimurium LT2 was amplified by polymerase chain reaction (PCR) using the genomic DNA from *S.* Typhimurium LT2 as a template (72). The forward and reverse primers were 5' - GAT TA GGA TCC CAT GTT ATC AGC CGA AAA CCG-3' /5' -GAT TA CCG CTC GAG TTA CTC GAT GAA GGC ATC TGC T-3' respectively. The restriction enzyme site of *BamHI* used for cloning is underlined. Plasmid mutagenesis of Asp61 to Ala61, Asn65 to Ala65, Arg68 to Ala68, His88 to Ala88 and Tyr91 to Ala91 was performed using an EZchange Site-directed Mutagenesis Kit (Enzynomics, Republic of Korea).

2.2.2. Protein expression and purification

Two recombinant plasmids of pET-21a(+)-SehB and pET-

28a(+)-SehA were co-transformed into *Escherichia coli* strain Rosetta2(DE3)pLysS. The recombinant proteins SehA and SehB were overexpressed in Rosetta2(DE3)pLysS cells using Luria Broth culture medium. Protein expression was induced upon cell growth reaching the mid-log phase by 0.5 mM isopropyl 1-thio-β-D-galactopyranoside and the cells were further incubated for additional 4 hours at 37° C. The cells were harvested by centrifugation at 5600 g for 10min. The harvested cells were lysed by sonication in lysis buffer [50mM Tris-HCl, pH 7.5, 500 mM NaCl, 1 mM phenylmethylsulfonyl fluoride, 10% (v/v) glycerol, and EDTA-free, Complete Protease Inhibitor Cocktail (Roche Diagnostics)] and centrifuged at 17,900 g for 1h. The supernatant was filtered by 0.45 μm pore size membrane (Millex-HV filter unit, Millipore, USA) to remove remnant debris and facilitate purification process. The filtered supernatant was applied to a Hitrap chelating column (GE Healthcare) which was previously equilibrated with buffer A (50 mM Tris-HCl, 500mM NaCl, pH 7.5). In the step, both SehA and SehB proteins were eluted in one peak with a linear gradient of 0-0.5 M

imidazole in buffer A with 10% (v/v) glycerol. Both SehA and SehB proteins were further purified by gel filtration on a HiLoad 16/60 Superdex 200 prep-grade column (GE Healthcare), which was previously equilibrated with buffer A with 200 mM NaCl. Fractions containing both SehA and SehB proteins were eluted in a single peak and were concentrated to 20 mg/ml for crystallization using an Amicon Ultra-15 centrifugal filter unit (Millipore). The recombinant SehAB complex substituted with selenomethionine (SeMet) was expressed and purified nearly identical to the steps of native SehAB complex, except M9 cell culture medium containing SeMet was used. The protein concentration for SehA and SehB complex was estimated by measuring the absorbance at 280 nm, employing a calculated extinction coefficient of 25,900 $M^{-1}cm^{-1}$. The gene coding for SehA and SehA mutants were cloned into pET32a vector (Novagen) to obtain soluble *S.* Typhimurium LT2 SehA and SehA mutant proteins for in vitro ribonuclease test. The plasmids with the SehA and SehA mutants insert were transformed into *E. coli* BL21 cell. Protein overexpression was induced by 0.5 m*M* IPTG when the cells grown

at 37° C reached the mid-log phase, and the cells were incubated for an additional 24 h at 15° C. The cells were harvested by centrifugation at 5,600 g and then lysed by sonication in buffer B (50 mM Tris-HCl, 500mM NaCl, pH 7.9) containing protease inhibitor cocktail tablets (Roche), and then centrifuged to remove cellular debris at 17,900 g. The supernatant was applied to a Hitrap chelating column, (GE Healthcare) which was previously equilibrated with buffer B. The protein was eluted with buffer B containing 500 m*M* imidazole and the eluted sample was further purified by size-exclusion chromatography step using a Superdex 200 10/300 pre-packed column (GE Healthcare) previously equilibrated with buffer B containing 200mM NaCl. Fractions contacting SehA and SehA mutant proteins were eluted in a single peak and concentrated to 1 mg/ml using Amicon Ultra-15 centrifugal filter unit (Milipore) in preparation for in vitro ribonuclease test. The recombinant SehB and truncated SehA complex was expressed and purified as described above except that cells grown at 37° C reached the mid-log phase, and the cells were incubated for additional 4hr at 37° C.

2.2.3. Crystallization and X-ray data collection

Crystallization of both native and SeMet-substituted SehAB complex was performed at 20°C by sitting-drop vapor diffusion method. Initial crystallization conditions were established using screening kits from Hampton Research and Emerald Bio. Each sitting drop was prepared by mixing 0.5 μl of the protein solution (20 mg/ml protein concentration in 50 mM Tris-HCl, pH 7.5, and 200 mM NaCl for native protein; 15 mg/ml for SeMet-substituted protein) and 0.5 μl of the reservoir solution and was placed over 80 μl of the reservoir solution. Both native and SeMet-substituted crystals were produced within a week to maximum dimensions 0.1 × 0.2 × 0.1 mm at 20°C. The reservoir solution supplemented with 20% (v/v) glycerol was used to vitrify both crystal samples. Crystals were soaked in the cryoprotectant solution for a few minutes before being placed in liquid nitrogen. Best crystals of SeMet-labeled *M. tuberculosis* VapBC30 were obtained in the reservoir solution of 2.0 *M* ammonium sulfate and 0.1 *M* sodium acetate trihydrate at pH 4.6. Best crystals

of native *M. tuberculosis* VapBC30 were obtained in the reservoir solution of 0.1 *M* bis-tris pH 5.5, and 2.0 *M* ammonium sulfate. X-ray diffraction data of native crystal and a set of single-wavelength anomalous diffraction (SAD) data from SeMet-substituted crystal were collected at 100 K using a Quantum 315r CCD area detector (Area Detector Systems Corporation, Poway, CA, USA) at the BL-5C experimental station of Pohang Light Source, Korea. Native crystal of the SehAB complex belonged to the orthorhombic space group $P2_12_12_1$, with unit cell parameters of a = 56.92 Å, b = 117.36 Å, c = 234.40 Å, $\alpha = \beta = \gamma = 90^\circ$. The SeMet crystal of the SehAB complex belonged to the orthorhombic space group $P2_12_12_1$, with unit cell parameters of a = 57.04 Å, b = 117.73 Å, c = 235.41 Å, $\alpha = \beta = \gamma = 90^\circ$. Raw data were processed and scaled using the HKL2000 program package (73).

2.2.4. Structure determination, refinement, and analysis

A set of SAD data from a crystal of the SeMet-substituted SehAB complex was used to solve the phase problem. Selenium

atoms were located and the phases were calculated with the PHENIX AutoSol (74). Initial model building was also carried out using the PHENIX AutoBuild (74). Model building and addition of water molecules were manually performed using the program Coot (75). The model was refined with the program Refmac (76), including the bulk solvent correction. 5% of the data were randomly set aside as the test data for the calculation of R_{free} (77). The refined model was evaluated using MolProbity (78) and RCSB validation server (http://www.wwpdb.org/). 98.03% of the modeled residues lie in favored regions of the Ramachandran plot with no outliers. Structural deviation was calculated using Superpose (79). Solvent accessible surface areas were calculated using *PISA* (45) and Protein Interactions Calculator (80).

2.2.5. *in vitro* ribonuclease assay

The SehA and mutated *S*ehA with thioredoxin tag were characterized in terms of cleavage RNA activity using the fluorescence quenching assay by RNase Alert kit (IDT). For

the assay, 33 μM SehA (or SehAB, SehB-SehA_truncated) and mutants, buffer B with 200mM NaCl were included in 70 μl reaction solutions. Subsequent fluorescence was recorded at 520 nm after excitation at 490 nm per minute for 1 h. Negative control contained buffer B with 200mM NaCl, and the RNaseAlert buffer of the kit content. In this assay system, a fluorophore is covalently linked to one end of synthetic RNA strand and quenched by the neighboring quencher group at the other end. When ribonuclease is added to the synthetic RNA with a fluorophore-quencher pair, the RNA is then digested to allow the separation of fluorophore and quencher, causing an elevation of fluorescence, which can be detected at 520 nm absorbance after excitation at 490 nm by fluorometer. The resulting fluorescence (RFU) was monitored on a SPECTRA max GEMINI XS spectrofluorometer.

2.3. Results and discussions

2.3.1. Structure determination and model quality

The phase problem was solved using SeMet SAD data collected at 2.80 A. The model of *S.* Typhimurium LT2 SehAB was refined to R_{work}/R_{free} values of 21.5/23.8% for the 30.0 Å – 2.49 Å data using a native set of the SehAB crystal. Our model of *S.* Typhimurium SehAB complex is composed of toxin SehA and antitoxin SehB, which contains four heterodimers of SehAB complex in an asymmetric unit of the crystal. The model of the native SehAB includes a total of 403 amino acid residues for SehA (residues 1 – 103 for chain E; residues 1 – 100 for chains F, G, and H) and 576 amino acid residues for SehB (residues 4 – 147 for chains A, B, C, and residues 7 – 147 for chain D) and 136 water molecules in the crystallographic asymmetric unit. In the native SehAB complex model, portions of the C-terminal residues (three residues in chains F, G, and H) of toxin SehA and N-terminal residues [1-3 residues (chains A, B, C, and D)] of antitoxin SehB, as well as the N-terminal hexa-histidine tags are missing.

These portions are likely to be disordered in the crystal. Four SehA/SehB monomers in the asymmetric unit are highly similar to each other, with r.m.s. deviations of 0.39–0.74/0.63–1.21 Å for 100/142–144 C_α atom pairs. Since all of the four heterodimers are similar in the asymmetric unit of the crystal, we will use chains A/E as a representative SehAB complex.

2.3.2. Overall structure of *S.* Typhimurium SehAB complex

In the asymmetric unit of crystal, the heterotetramer of two SehAB complex has approximate dimensions of 65 Å × 80 Å × 45 Å, with interface areas of 1,340–1,350 $Å^2$ between two SehAB complexes and 1,500–1,610 $Å^2$ between toxin SehA and antitoxin SehB. The database analysis by *PISA* server shows Complexation Significance Score (CSS) of 1.0 (between two SehAB complex) and 1.0 (between SehA and SehB in the complex), respectively (45), implying that heterotetramer or heterodimer form of SehAB complex can stably form the complex in solution, consistent with that in the crystal. In the SehAB complex models of the crystal, the SehA and

SehB models are related by internal pseudo-two-fold symmetry. Overall, two SehAB complexes form arch-shaped architectures, which are formed by interactions of two SehB from each SehAB complex (Figure 20). The interactions between each SehB from two SehAB complexes are made mainly by three α-helices (α1, α2, and α3) at the N-terminus of chains A and B (or chains C and D), while the C-terminus of both SehB are separated from each other by 20 - 22 Å. The C-terminal DNA-binding domains (HTH motif) of SehB antitoxins are facing towards the opposite side of each N-terminal interaction domain.

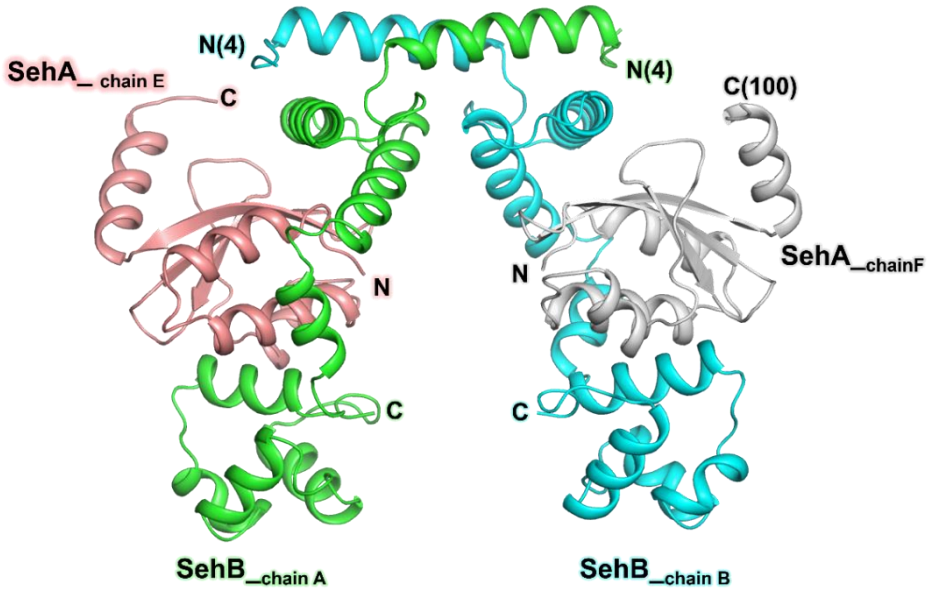

Figure 20. Overall structure of SehAB from *Salmonella enterica* serovar Typhimurium LT2. heterotetrameric SehAB complex. Ribbon representation of the SehAB heterotetramer of the crystal. The models of the SehA toxin are shown as salmon and gray (chains E and F, respectively). The models of the SehB antitoxin are shown as blue and cyan (chain A and B, respectively).

2.3.3 Structure of SehA toxin

Discussion only on chain E will be made since all four SehA monomers in the asymmetric unit are highly similar to each other with r.m.s. deviations of 0.3–0.6 Å for 100 Cα atom pairs. Among chain E–H, only three more residues (GLN101–GLU103) in chain E existed. The toxin SehA is composed of single folded domain and is comprised of an $\alpha/\beta/\alpha$ fold constituted by five antiparallel β-strands of the small and large β-sheets arranged in the order of $\beta 2\uparrow-\beta 3\downarrow-\beta 4\uparrow-\beta 5\downarrow-\beta 1\downarrow$, flanked by one α-helix on one side and three α-helices on the other side (Figure 21A). The consecutive four β-strands ($\beta 2-\beta 5$) run antiparallel to each other whereas β 1 runs parallel to the adjoining $\beta 5$ strand and forms the five-stranded mixed β-sheet. Structural homologs of SehA were searched using the DALI server and several matches were obtained (Figure 21B). All belonged to the RelE/YoeB family of bacterial ribonuclease from various organisms, but their sequence identity between homologs of SehA and SehA was low. These homologs have central antiparallel β-sheet and adjacent α-helix similar to SehA.

The results of DALI server (81) search showed that SehA toxin is most similar to (i) the HigB toxin from *Escherichia coli* (82) [PDB code 5IFG; Z−scores of 18.2, and sequence identity of 40%] , (ii) the RelE toxin from *Methanococcus jannaschii* (83) [PDB code 3BPQ; Z−scores of 9.4, and sequence identity of 21%], (iii) the YafQ toxin from *Escherichia coli* (84) [PDB code 4ML0; Z−scores of 8.3 and sequence identity of 12%], (iv) other RelE toxin from *Pyrococcus horikoshii* (85) [PDB code 1WMI Z−scores of 8.2 and sequence identity of 14 %], (v) the HigB toxin from *Proteus vulgaris* (86) [PDB code 4MCT; Z−score of 8.1, and sequence identity of 9%], (vi) the uncharacterized toxin from *Helicobacter pylori* (87) [PDB code 4LTT; Z−score 8.0 and sequence identity of 18%], (vii) another RelE toxin from *Escherichia coli* (88) [PDB code 4FXE; Z−scores of 7.1 and sequence identity of 10%] (viii) the toxin YoeB form *Escherichia coli* (89) [PDB code 2A6R; Z−scores of 6.5 and sequence identity of 12%]. Overall the structure of SehA toxin seemed similar to other homologues, but dissimilar discrete structural features between SehA and SehA homologs were observed

based on DALI server results. Compared with homologs of SehA and SehA, SehA toxin had intact α helix on C-terminal, while C-terminal α helix was not present in homologs of SehA or was present as a loop or short helix (Figure 21C). In addition, the distances between the C-terminus and the central beta strand of RelE and YoeB from *E. coli* differed in the antitoxin bound and unbounded form (90). The C-terminal helix of SehA was longer than the C-terminal of homologs and the C-terminal of homologs underwent structural change upon binding of the antitoxin. Therefore, an assumption can be made in the sense that the C-terminal of SehA affects the activity of SehA.

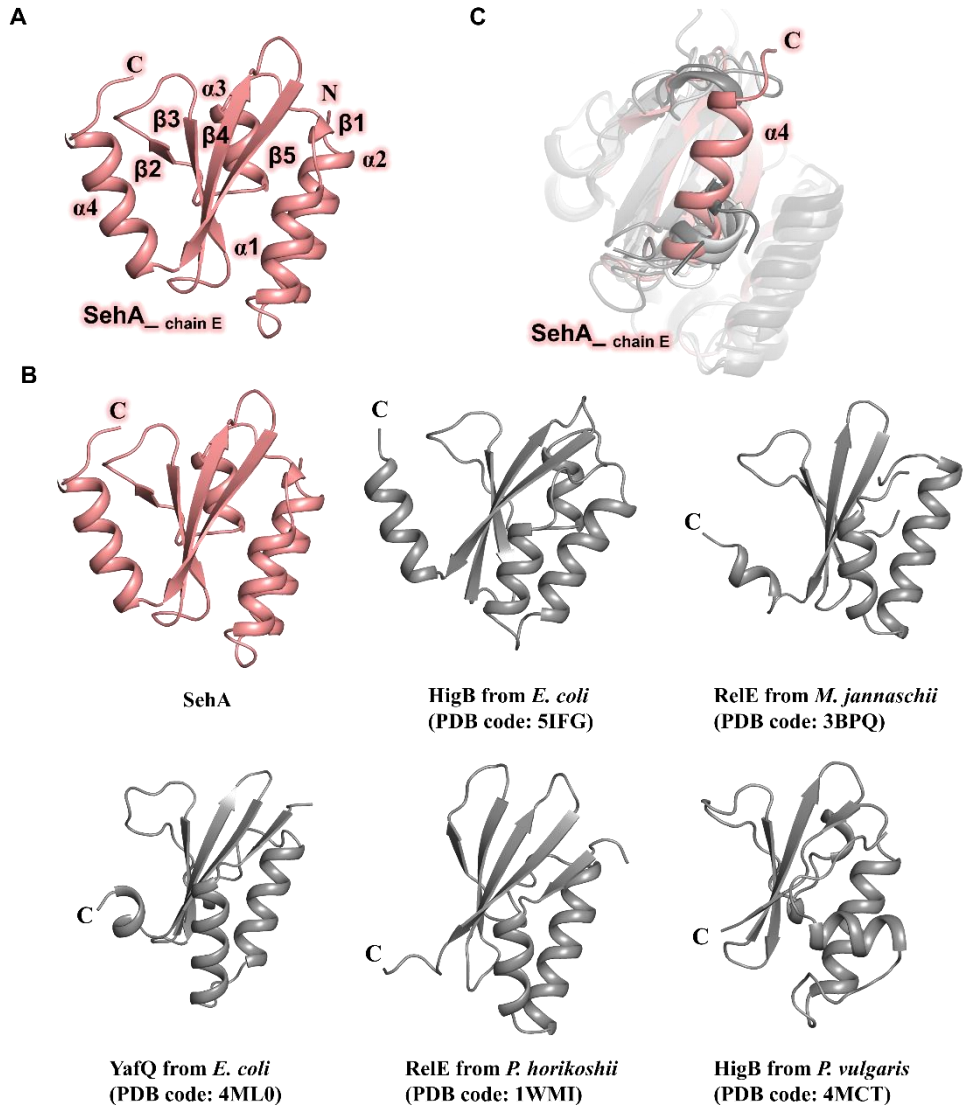

Figure 21. Structure of SehA toxin and its homologs (A) The SehA toxin is indicated by a ribbon representation, (B) SehA homologs are indicated by a ribbon representation, (C) Superimpose with SehA and homologs, SehA is shown as salmon, and homologs are shown as gray.

2.3.4 SehA toxin as ribonuclease

The SehA shares structural features of the RelE family, but the active site residues were not known. Thus, the active sites of the SehA homologs were investigated to predict the putative active residues of SehA. In order to test which residues play a role in SehA-mediated toxicity, mutagenesis experiment with a fluorescence quenching assay was employed. Based on results of superimposition between SehA and homologs of SehA, five potential active residues of SehA including Asp61, Asn65, Arg68, His88 and Tyr91 were selected (Figure 22A). As a result, the SehA mutants N65A and R68A showed similar toxicity to SehA wild type, D61A and Y91A showed increased toxicity and H88A showed less toxicity compare to the SehA wild type (Figure 23A). According to previous studies, the distance between the C-terminal and the central beta strands of the toxin was longer when the antitoxin was bound to the toxin compared to its free, unbound form (90). The position of the C-terminal alpha helix was also near the putative active site residues of the SehA toxin. Taken together, the C-terminal helix was thought

to affect the activity of the SehA toxin, and therefore, ribonuclease assay using fluorescence quenching assay was performed to observe the effect of the C-terminal helix on the activity of the SehA toxin. Considering the difficulties of wild type toxin purification and results of previous studies, ribonuclease assay was carried out with the C-terminal helix truncated toxin and the antitoxin complex. As a result, the wild type SehAB complex showed no ribonuclease activity, whereas the truncated SehA and SehB complex showed strong ribonuclease activity despite the binding of SehB antitoxin to the truncated SehA toxin (Figure 23B). Based on these results, it can be assumed that the C-terminal helix of SehA may influence the ribonuclease activity of SehA. To further investigate the effect of the C-terminal helix of SehA on its activity, the residues that form intrainteraction with the C-terminal helix in the SehA toxin was observed. Specifically, Arg54 and Asp55 on the $\beta 2-\beta 3$ loop of SehA interacted with Tyr98, Asn101 and Asp103 on the C-terminal helix of SehA (Figure 22B). In order to investigate the effect of the interaction between Arg55, Asp54 and the C-terminal alpha helix on

the activity of SehA toxin, Arg54 and Asp55 was mutated and mutation site was gradually widened. The ribonuclease assay was also proceeded with SehB antitoxin bound to mutated SehA toxins. As a result, it was observed that the ribonuclease activity became stronger as the mutation site was widened (Figure 23C). Based on the ribonuclease assays that mutated the C-terminal alpha helix of the toxin, the C-terminal helix and the ribonuclease activity of SehA toxin were closely related. The results of ribonuclease assay that mutation of putative active site residues of SehA toxin, specifically Asp61 and Tyr91 of SehA toxin showed stronger ribonuclease activity than wild type SehA toxin. Associate with results of C terminal related ribonuclease assays, Asp61 and Tyr91 residues were assumed to affect the interaction between C-terminal helix and SehA toxin rather than actual active site residues. Based on ribonuclease assays of SehA toxin, the ribonuclease activity of the toxin was observed and the C-terminal helix of SehA toxin directly affected the ribonuclease activity of the SehA toxin.

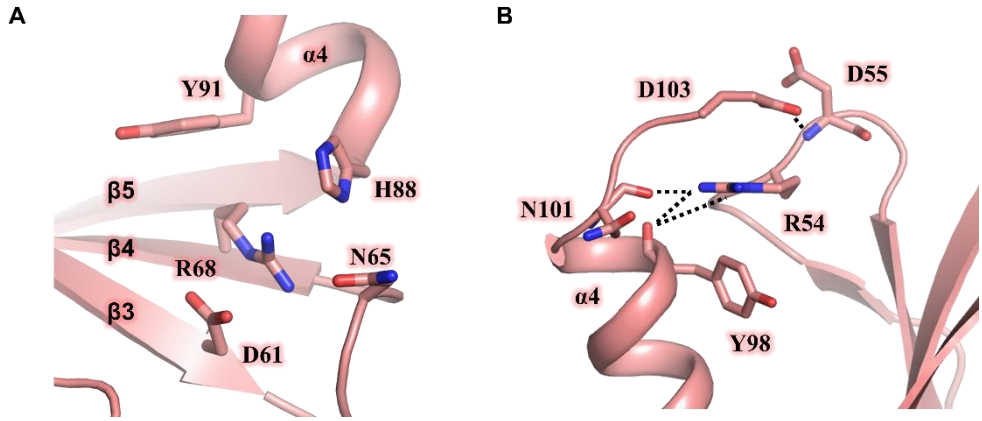

Figure 22. Structure of SehA toxin active site and intrainteraction with C-terminal alpha helix of SehA toxin (A) The putative active site residues are shown in the stick models. (B) The Interacting residues of SehA toxin are shown in stick models. The hydrogen bonds and salt bridges are shown as the black dotted lines.

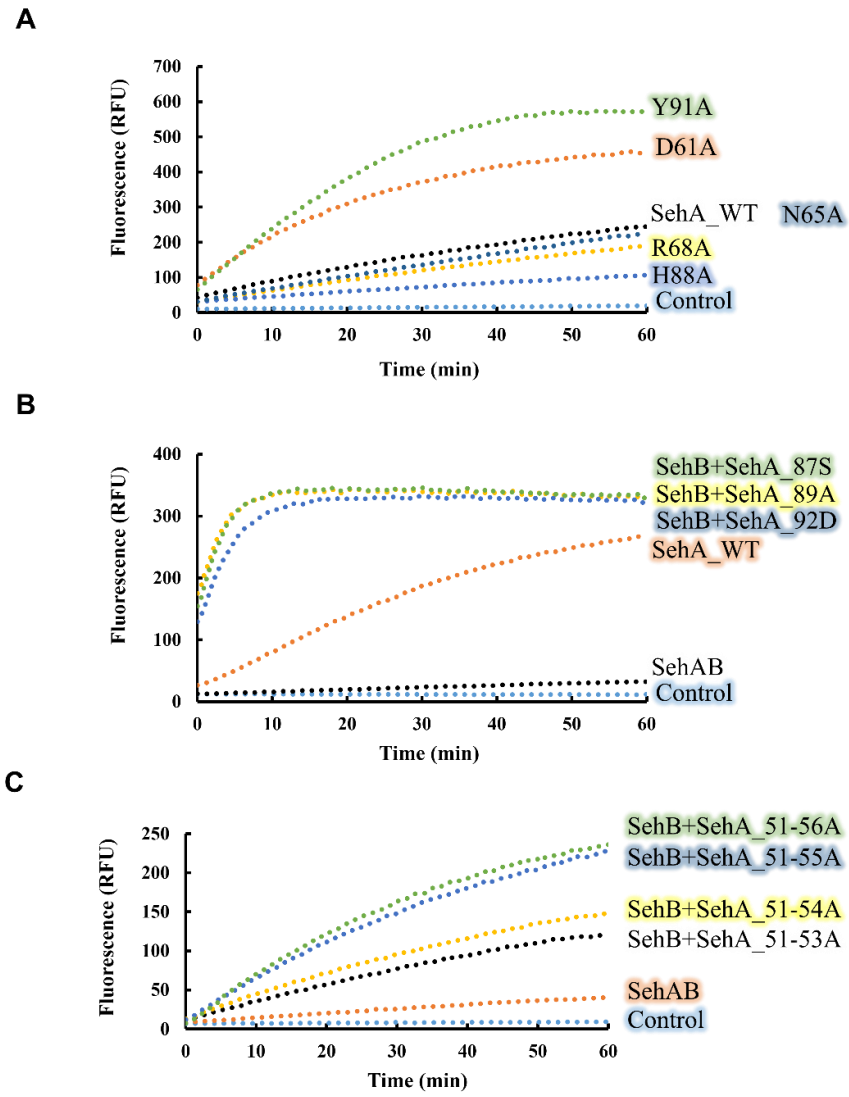

Figure 23. Ribonuclease assays of SehA toxin (A) Mutation putative active site residues of SehA toxin, (B) The SehB antitoxin with C-terminal alpha helix truncated of SehA toxin, (C) Mutation residues that contributed intrainteraction between SehA toxin and C-terminal alpha helix of SehA toxin. *In vitro* ribonuclease assays were performed as described in the 'Materials and methods' section. Each experiment was performed in triplicate. Fluorescence was reported every 30 sec for 60 min.

2.3.5 SehB antitoxin

Similar to SehA, four SehB monomers in the asymmetric unit are also highly similar to each other with r.m.s. deviations of 0.69–1.22 Å for 142–144 C_α atom pairs. The SehB antitoxin consists of 148 amino acids. In the SehAB structure, three antitoxin proteins showed 144 residues out of 148 residues and the residual antitoxin showed 142 residues out of 148 residues. As a whole SehB antitoxin contained eight α-helices in an ordered fashion. The N-terminal α1 (residues 9 - 24) helix which was in perpendicular position to α2 - α3 helices, dimerizes with neighboring antitoxin α1-α3 helixes. The midmost of SehB antitoxin structure, which consists of four α-helices including α2, α3, α4 (residues 74 - 85), and α5 (residues 90 - 100), form the cleft in which the SehA toxin binds via hydrogen bonds, salt bridges, and hydrophobic interactions. The C-terminal helix cluster of SehA antitoxin including α6 (residues 104 - 111) helix, α7 (residues 114 - 122) helix, and α8 (residues 129 - 139) helix, also called as the HTH motif, are well structured. Although minor differences exist between the four monomers, overall

structure is very similar; thus, only chain A will be discussed. The DALI server results showed the homologs that have the HTH (Helix−Turn−Helix) motif. The homologues that showed (81) highest similarity is (i) the HigA antitoxin from *Escherichia coli* (82) [PDB code 5IFG; Z−scores of 10.1, and sequence identity of 36%] (ii) PLI0006 PROTEIN from *Listeria innocua*(to be published) [PDB code 3OP9; Z−scores of 8.6 and sequence identity of 13%], (iii) the Putative HTH−type transcriptional regulator YBAQ protein from *Escherichia coli* (to be published) [PDB code 2EBY; Z−scores of 7.6 and sequence identity of 16%], (iv) the restriction−modification controller from *Aeromonas hydrophila* (91) [PDB code 1Y7Y; Z−scores of 7.3 and sequence identity of 9%], (v) the P22 c2 repressor protein from *Enterobacteria phage* (92) [PDB code 3JXC; Z−scores of 7.2 and sequence identity of 15%], (vi) the prgX −negative regulator from *Enterococcus faecalis* (93), [PDB code 2GRL; Z−score of 7.1 and sequence identity of 18%], (vi) the master regulator for biofilm from *Bacillus subtilis* (94) [PDB code 3ZKC; Z−score of 7.1 and sequence identity of 10%], (vii) the antitoxin Hig A from

Escherichia coli (to be published) [PDB code 2ICP; Z-score of 6.9 and sequence identity of 7%]. The structure of SehB could be divided into three parts based on their roles: The N-terminal of SehB contribute dimerization of SehB, the midmost portion of the SehB binds to SehA toxin and the C-terminal HTH domain binds to DNA (Figure 24A). Specifically, there are hydrophilic interactions between the SehB dimer: interactions of (i) Arg5 on N-terminal loop with Asn36 and Arg40 on the α2 helix, (ii) Glu60 and Arg65 on the α3 helix with Glu60 and Arg65 on the α3 helix (Figure 24B). Additionally, there are hydrophobic interactions between the SehB dimer: interactions of (i) Ala22 and Val23 on the α1 helix with Phe19 and Ala22 on the α1 helix, Pro57 on the α3 helix, (ii) Val26, Pro27 and Met29 on the α1-α2 loop with Met7 on the N-terminal loop, Ile15 and Phe19 on the α1 helix and Pro57 on the α3 helix, (iii) Ala43, Leu44, Phe47 and Leu48 on the α2 helix with Met7 on the N-terminal loop and Ala9, Ala12, Ile15 and Val16 on the α1 helix, (iv) Pro57, Leu58 and Leu61 on the α3 helix with Val16, Phe19 and Val21 on the α1 helix, Met29 on the α1-α2 loop, Pro57

and Leu61 on the α3 helix (Figure 24C). SehB dimerization might possibly be driven mainly by hydrophobic interactions within the dimer interface because the number of residues involved in hydrophobic interactions is larger than that of residues involved in hydrophilic interactions.

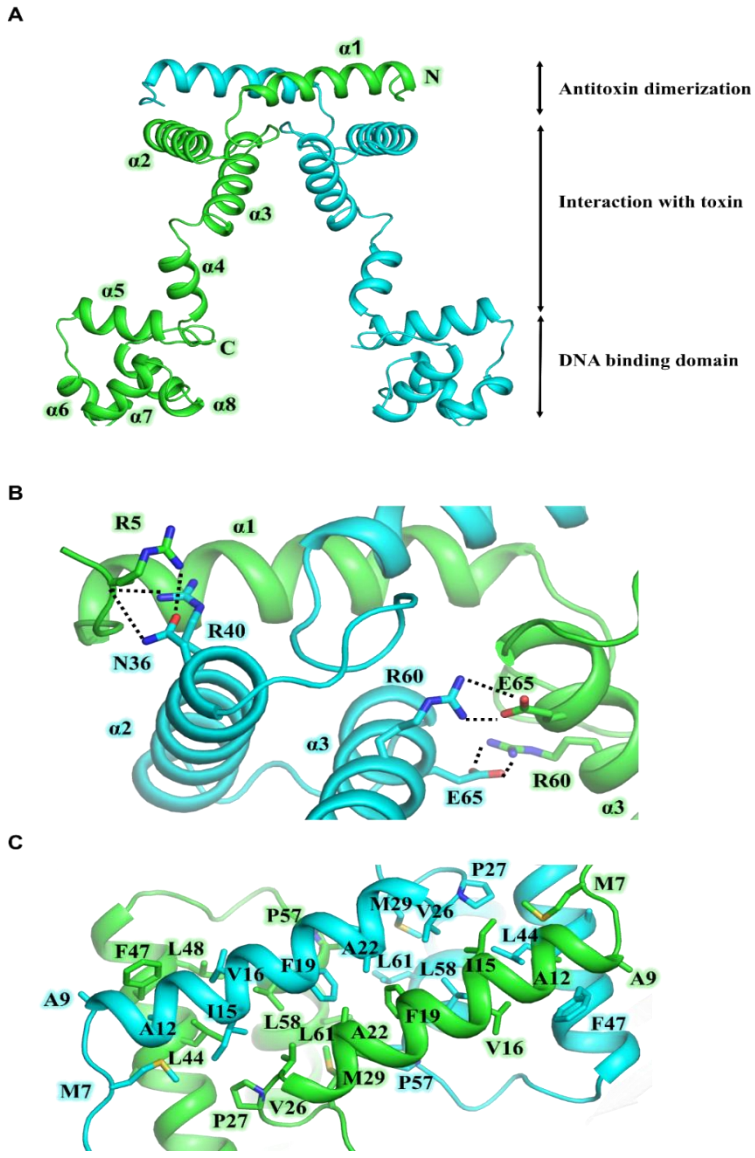

Figure 24. Structure of SehB antitoxin (A) The three parts are divided based on the roles of the antitoxin. The SehB antitoxin is indicated by a ribbon representation. (B & C) The residues involved in the hydrophilic and hydrophobic interactions of SehB antitoxin dimer. The hydrogen bonds and salt bridges are shown as the black dotted lines, and the residues participating in the interactions are shown in the stick models.

2.3.6 Interaction between SehA toxin and SehB antitoxin

In SehAB complex structure, the toxin SehA is wrapped around by the SehB antitoxin (Figure 25A). Specifically, there are hydrophobic interactions between SehB and SehA: (i) Val49 on the α2 helix with Ile4 on the β1 – α1 loop, Tyr72 on the β4 strand and Phe81 on the β5 strand, (ii) Leu54 on the α2 – α3 loop with Tyr72 on the β4 strand and Leu77 on the β4 – β5 loop, (iii) Ile66 on the α3 helix with Ile4 on the β1 – α1 loop, (iv) Leu79 and Leu83 on the α4 helix with Phe9 and Met13 on the α1 helix, Leu27 on the α1 helix, (v) Val92 and Tyr100 on the α5 helix with Val29 on the α2 helix, Tyr44 on the α3 helix and Pro46 on the α3 – β2 loop and (vi) Leu141, Pro142 and Ala145 on the C-terminal loop with Tyr44 on the α3 helix and Pro46 on the α3 – β2 loop (Figure 25B). Additionally, there are hydrophilic interactions between the SehB and SehA: (i) Glu46 and Asp50 on the α2 helix with Lys83 on the β5 strand, (ii) Glu70 on the α3 helix with Ser5 and Arg6 on the α1 helix, (iii) Glu75, Asn80, His82 and Leu83 on the α4 helix with Arg6 and Asn10 on the α1 helix, Glu20 and Asn28 on the α2 helix,

(iv) Thr86 on the $\alpha 4 - \alpha 5$ loop with Glu25 on the $\alpha 2$ helix, (v) Ser91, Arg94, Asp98 and Gln99 on the $\alpha 5$ helix with Glu25 and Asn28 on the $\alpha 2$ helix, Ser47 on the $\alpha 3 - \beta 2$ loop, Asp61 and Ser63 on the $\beta 3$ strand and (vi) Lys140 and Asp144 on the C-terminal loop with Lys33 on the $\alpha 2 - \alpha 3$ loop and Arg43 on the $\alpha 3$ helix (Figure 25C). One of striking features of SehAB complex structure was that the active site of SehA faced towards the solvent channel, which was distant from SehB and thus was unlikely to be blocked by SehB. Previous studies on TA complex structures including HigAB from *P. vulgaris* and MqsAR from *E. coli* also showed that antitoxins did not occupy or directly disrupt their active sites during formation of each complex. However, a process of antitoxin to inactivate its cognate toxin is blocking the interaction between toxin and other biomolecules, such as the ribosome (86,95). The interaction between the SehA toxin and the SehB antitoxin was similar in the way that the antitoxin did bind to the active site of the toxin, but compared to the HigAB and MqsAR complex, SehB encompassed toxins more tightly. In both HigAB and MqsAR complex,

only two region contacts were made while three regional contacts were made between SehA toxin and SehB antitoxin. However, the RelBE complex from *P. horikoshii*, *E. coli*, and *M. jannaschii*, and DinJ-YafQ from *E. coli*, demonstrated that antitoxins penetrated into their cognate toxin active site (83-85,88)(Figure 26). SehAB interaction has a unique binding mode that is different from other homologs. In the ribonuclease assay, the weakened intrainteraction between toxin and C-terminal alpha helix, and loss of the SehA toxin C-terminal helix were shown to exhibit robust ribonuclease activity. Additionally, antitoxin controls the activity without penetrating the putative active site of the toxin. It is considered that the antitoxin tightly binds the toxin to change the position of the C-terminal helix of the toxin or to control the activity of the toxin by changing the structure of the toxin.

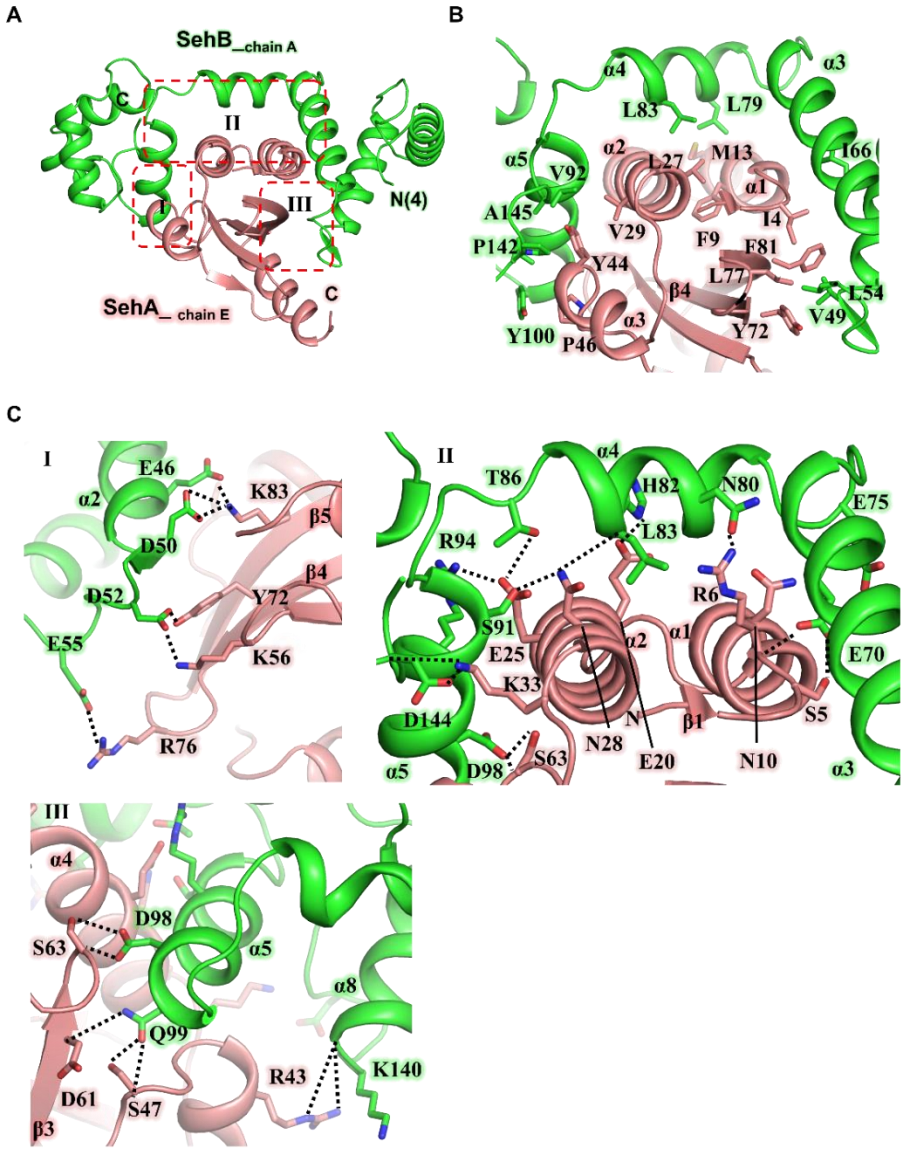

Figure 25. Analysis of interaction between SehA and SehB (A) The region of interaction is indicated by the red dotted rectangles. (B and C) The residues involved in the hydrophilic and hydrophobic interactions between the SehB antitoxin and SehA toxin. The hydrogen bonds and salt bridges are shown as the black dotted lines, and the residues participating in the interactions are shown in the stick models.

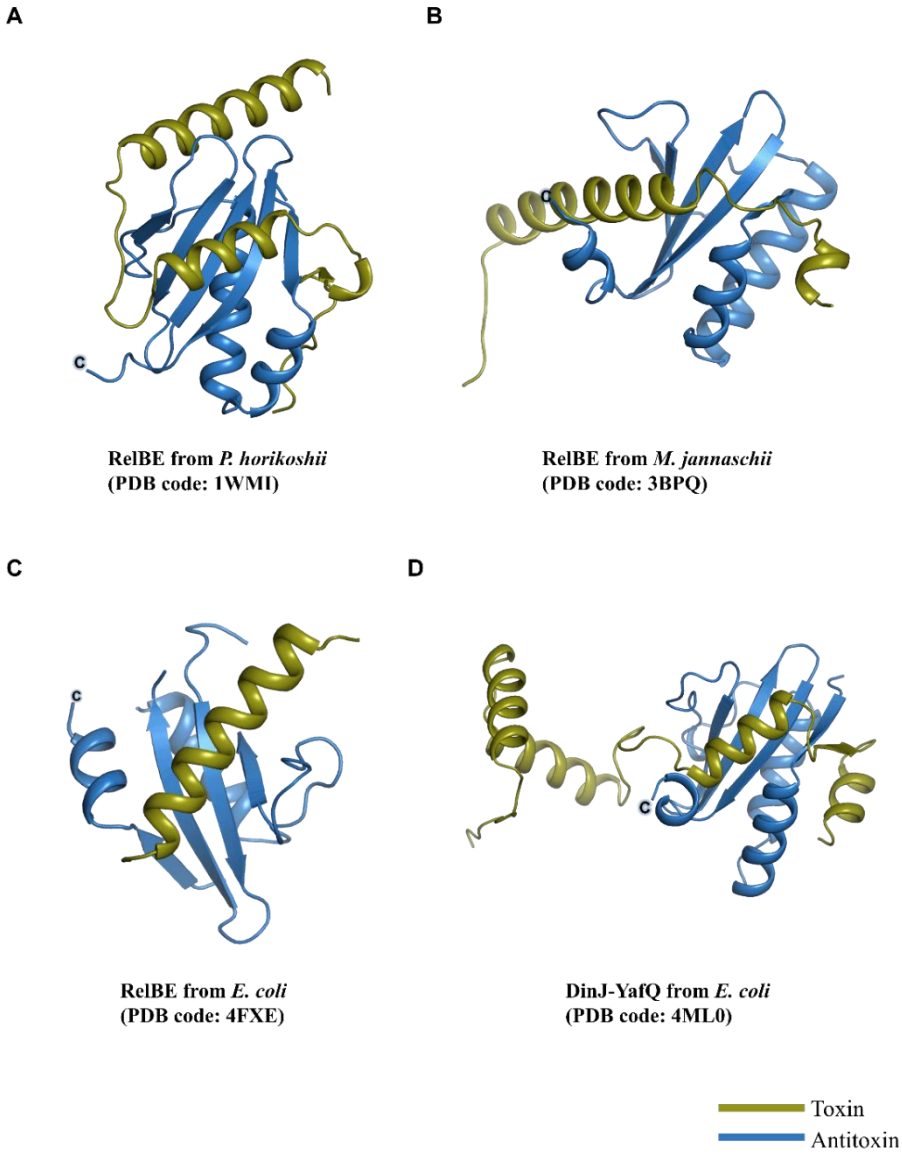

Figure 26. The structure of SehAB homologs. (A, B, C and D) Structures of homologs of SehAB [*Pyrococcus horikoshii* RelBE (PDB code 1WMI); *Methanococcus jannaschii* RelBE (PDB code 3BPQ); *Escherichia coli* RelBE (PDB code 4FXE); *Escherichia coli* DinJ-YafQ (PDB code 4ML0)]. The models of toxins and antitoxins are colored in blue and dark green, respectively.

2.4. Conclusion

The toxin-antitoxin system has been attracting attention as a new antibiotic target due to its role in the cell and its mechanism of action. There exist at least 14 type II toxin-antitoxin systems in *Salmonella enterica* serovar Typhimurium LT2, and there is no known structure yet. Although the SehAB complex has been shown to be active in cells, there is no structural information. The structure of SehAB complex structure was determined at 2.49 Å resolution. The SehAB complex showed that the SehB antitoxin tightly surrounded the SehA toxin. The SehB antitoxin formed a dimer at the N-terminal, DNA-binding domain at the C-terminal, and interaction with the SehA toxin occurred in the middle of the antitoxin. SehA toxin is known as the RelE family, the C-terminal alpha helix is intact and long in comparison to the homologs. The C-terminal alpha helix of the SehA toxin is located near the putative active site of the SehA toxin and have been shown to be an important factor in the activity of the toxin as a result of ribonuclease assays. Unlike other homologs,

the SehAB complex has a binding mode in which the SehB antitoxin tightly surrounds the SehA toxin without penetrating the putative active site of the toxin. The results of the ribonuclease assays and the comparison to other homologs suggested that the binding of the antitoxin to the toxin may change the structure of the C-terminal alpha helix of toxin or structure of the toxin and control the activity of the toxin. The unique binding mode of SehAB will broaden the spectrum and understanding of the toxin-antitoxin structure and will contribute to the production of potential antibiotic candidates in the future.

Summary

In this study, we performed a structural and functional studies on the VapBC complex and the SehAB complex from *Salmonella enterica* serovar Typhimurium LT2. When the cells are exposed to a stressful environment, the antitoxin is degraded and the activity of the toxin causes the cell death or cell growth retardation. This mechanism is being watched as a target of new antibiotic candidates. Our goal is the development of new antibiotic candidates using toxin-antitoxin system, and the first step is to obtain the structure of toxin-antitoxin complex and to conduct functional studies based on the obtained structure.

In the chapter 1, structural and functional studies of the VapBC complex from *S.* Typhimurium LT2 type II toxin antitoxin systems, were performed. The VapBC complexes consist of VapC, which exhibits metal-dependent ribonuclease activity, and VapB antitoxin, which inhibits the VapC activity via the C-terminal of VapB and regulates transcription of VapBC using a DNA biding motif located at

the N-terminal. In this work, we solved the crystal structures of the VapBC complex from *S.* Typhimurium LT2 in DNA-free and -bound states at 2 Å and 2.8 Å, respectively. Based on the DNA-free VapBC structure, we could observe how VapB antitoxin inhibits the activity of VapC toxin and how VapB and VapC are bind. Also, since toxin-antitoxin transcription is regulated by DNA-binding motifs in antitoxin, their relationship between DNA and toxin-antitoxin complex is crucial to understand of toxin-antitoxin system. We were determined the DNA bound-VapBC structure and obtained an understanding of the interaction between toxin-antitoxin complex and DNA. The VapC toxin has a PIN domain that shows metal-dependent ribonuclease activity in the structure. However, previous studies did not find a suitable metal to induce the ribonuclease activity of VapC from *Salmonella*, so we were screened several metals for ribonuclease activity of VapC and we were assumed VapC from *Salmonella* has calcium-dependent ribonuclease activity.

In the chapter 2, structural and functional studies of the SehAB

complex from *S.* Typhimurium LT2 type II toxin-antitoxin systems, were performed. The SehAB complex is known to be one of RelBE family which show ribosome-dependent ribouclease activity. Structural and functional studies of SehAB were carried out since no previous structural studies have been conducted. The SehAB complex consists of SehB antitoxin and SehA toxin. The SehA toxin has homologs of the RelE toxin and has a long and intact C-terminal helix when compared to its homologs. The C-terminal helix of the toxin is located near the putative active sites, thus suggesting that the C-terminal helix of the SehA toxin will have significant roles on the activity of the SehA and the experiment was carried out.

Ribonuclease assays showed that C - terminal helix of SehA toxin had a great effect on toxin activity. In addition, the SehB antitoxin inhibits the activity of SehA toxin without binding to the putative active sites of the SehA toxin and the C-terminal helix. Unlike the mechanism which the homologs antitoxin binds to the active site of the toxin and the C-terminal helix to inhibit the activity

of the toxin, the ribonuclease assay and structure of SehAB complex results suggest that SehB antitoxin inhibits the activity of SehA toxin by causing structural change of SehA toxin.

The goal of these studies are to develop an antibiotic peptide based on the structure of the toxin-antitoxin complex. There are three strategies for developing antibiotic peptides using the toxin-antitoxin complex structure.

The first strategy is that the peptide mimics the antitoxin which interferes TA complex, so that the peptide binds to the toxin instead of the antitoxin. Then, the separated antitoxin is degraded and the cell is killed by the remaining toxin activity. At this time, the peptide should not inhibit the activity of the toxin. The second strategy is a peptide that mimics the toxin. It is a peptide that interferes TA complex, binds to antitoxins, and uses the activity of isolated toxins to kill cells. The third strategy uses the mechanism which the antitoxin regulates the transcription of the toxin-antitoxin. When an antitoxin or TA complex bind to a specific DNA sequence in the

promoter region, the transcription of the toxin-antitoxin is stopped. When the peptide mimicking the DNA binding motif of the antitoxin binds to a specific DNA sequence in the promoter region, the toxin-antitoxin transcription is stopped, and relatively unstable antitoxin of the remaining TA complex is degraded, the free toxin kills the cell. In order to devise peptides using these three strategies, structural and functional information of toxin-antitoxin is essential and this study was conducted to obtain such information.

This study will contribute not only to the production of antimicrobial peptides but also to the development of toxin antitoxin studies.

Reference

1. Gerdes, K., Rasmussen, P.B. and Molin, S. (1986) Unique type of plasmid maintenance function: postsegregational killing of plasmid-free cells. *Proceedings of the National Academy of Sciences*, **83**, 3116-3120.
2. Ogura, T. and Hiraga, S. (1983) Mini-F plasmid genes that couple host cell division to plasmid proliferation. *Proceedings of the National Academy of Sciences*, **80**, 4784-4788.
3. Crump, J.A., Sjölund-Karlsson, M., Gordon, M.A. and Parry, C.M. (2015) Epidemiology, clinical presentation, laboratory diagnosis, antimicrobial resistance, and antimicrobial management of invasive Salmonella infections. *Clinical microbiology reviews*, **28**, 901-937.
4. Crump, J.A., Sjölund-Karlsson, M., Gordon, M.A. and Parry, C.M. (2015) Epidemiology, Clinical Presentation, Laboratory Diagnosis, Antimicrobial Resistance, and Antimicrobial Management of Invasive Salmonella Infections. *Clinical Microbiology Reviews*, **28**, 901-937.
5. Mogasale, V., Maskery, B., Ochiai, R.L., Lee, J.S., Mogasale, V.V., Ramani, E., Kim, Y.E., Park, J.K. and Wierzba, T.F. (2014) Burden of typhoid fever in low-income and middle-income countries: a systematic, literature-based update with risk-factor adjustment. *The Lancet Global health*, **2**, e570-e580.
6. Pui, C., Wong, W., Chai, L., Tunung, R., Jeyaletchumi, P., Hidayah, N., Ubong, A., Farinazleen, M., Cheah, Y. and Son, R. (2011) Salmonella: A foodborne pathogen. *International Food Research Journal*, **18**.
7. Snyder, M., Gonzalez, O., Palomino, C., Music, S., Hornick, R., Perroni, J., Woodward, W., Gonzalez, C., DuPont, H. and Woodward, T. (1976) COMPARATIVE EFFICACY OF CHLORAMPHENICOL, AMPICILLIN, AND CO-TRIMOXAZOLE IN THE TREATMENT OF. *The Lancet*, **308**, 1155-1157.
8. Winther, K.S. and Gerdes, K. (2009) Ectopic production of VapCs from Enterobacteria inhibits translation and trans-activates YoeB mRNA

interferase. *Molecular microbiology*, **72**, 918-930.

9. Winther, K.S. and Gerdes, K. (2011) Enteric virulence associated protein VapC inhibits translation by cleavage of initiator tRNA. *Proceedings of the National Academy of Sciences*, **108**, 7403-7407.
10. Winther, K.S. and Gerdes, K. (2012) Regulation of enteric vapBC transcription: induction by VapC toxin dimer-breaking. *Nucleic acids research*, **40**, 4347-4357.
11. Miguel, A., Zhao, W., Farenc, C., Gimenez, G., Raoult, D., Cambillau, C., Gorvel, J.-P. and Meresse, S. (2013) A toxin-antitoxin module of Salmonella promotes virulence in mice. *PLoS pathogens*, **9**, e1003827.
12. Vázquez-Laslop, N., Lee, H. and Neyfakh, A.A. (2006) Increased persistence in Escherichia coli caused by controlled expression of toxins or other unrelated proteins. *Journal of bacteriology*, **188**, 3494-3497.
13. Falla, T.J. and Chopra, I. (1998) Joint tolerance to β-lactam and fluoroquinolone antibiotics in Escherichia coli results from overexpression of hipA. *Antimicrobial agents and chemotherapy*, **42**, 3282-3284.
14. Korch, S.B. and Hill, T.M. (2006) Ectopic overexpression of wild-type and mutant hipA genes in Escherichia coli: effects on macromolecular synthesis and persister formation. *Journal of bacteriology*, **188**, 3826-3836.
15. Wang, X. and Wood, T.K. (2011) Toxin-antitoxin systems influence biofilm and persister cell formation and the general stress response. *Applied and environmental microbiology*, **77**, 5577-5583.
16. Yamaguchi, Y. and Inouye, M. (2011) Regulation of growth and death in Escherichia coli by toxin–antitoxin systems. *Nature Reviews Microbiology*, **9**, 779.
17. Van Melderen, L. and De Bast, M.S. (2009) Bacterial toxin–antitoxin systems: more than selfish entities? *PLoS genetics*, **5**, e1000437.
18. Coussens, N.P. and Daines, D.A. (2016) Wake me when it's over–Bacterial toxin–antitoxin proteins and induced dormancy. *Experimental Biology and Medicine*, **241**, 1332-1342.
19. Lee, K.-Y. and Lee, B.-J. (2016) Structure, biology, and therapeutic application of toxin–antitoxin systems in pathogenic bacteria. *Toxins*, **8**,

305.

20. Unterholzner, S.J., Poppenberger, B. and Rozhon, W. (2013) Toxin–antitoxin systems: Biology, identification, and application. *Mobile genetic elements*, **3**.
21. Guo, Y., Quiroga, C., Chen, Q., McAnulty, M.J., Benedik, M.J., Wood, T.K. and Wang, X. (2014) RalR (a DNase) and RalA (a small RNA) form a type I toxin-antitoxin system in Escherichia coli. *Nucleic Acids Res*, **42**, 6448-6462.
22. Brielle, R., Pinel-Marie, M.-L. and Felden, B. (2016) Linking bacterial type I toxins with their actions. *Current opinion in microbiology*, **30**, 114-121.
23. Gerdes, K. and Wagner, E.G.H. (2007) RNA antitoxins. *Current opinion in microbiology*, **10**, 117-124.
24. Wang, X., Lord, D.M., Cheng, H.-Y., Osbourne, D.O., Hong, S.H., Sanchez-Torres, V., Quiroga, C., Zheng, K., Herrmann, T., Peti, W. *et al.* (2012) A new type V toxin-antitoxin system where mRNA for toxin GhoT is cleaved by antitoxin GhoS. *Nat Chem Biol*, **8**, 855-861.
25. Aakre, C.D., Phung, T.N., Huang, D. and Laub, M.T. (2013) A bacterial toxin inhibits DNA replication elongation through a direct interaction with the β sliding clamp. *Molecular cell*, **52**, 617-628.
26. Masuda, H., Tan, Q., Awano, N., Wu, K.-P. and Inouye, M. (2012) YeeU enhances the bundling of cytoskeletal polymers of MreB and FtsZ, antagonizing the CbtA (YeeV) toxicity in Escherichia coli. *Molecular Microbiology*, **84**, 979-989.
27. Sevin, E.W. and Barloy-Hubler, F. (2007) RASTA-Bacteria: a web-based tool for identifying toxin-antitoxin loci in prokaryotes. *Genome biology*, **8**, R155.
28. Mruk, I. and Kobayashi, I. (2013) To be or not to be: regulation of restriction–modification systems and other toxin–antitoxin systems. *Nucleic acids research*, gkt711.
29. Park, S.J., Son, W.S. and Lee, B.J. (2013) Structural overview of toxin-antitoxin systems in infectious bacteria: a target for developing antimicrobial agents. *Biochimica et biophysica acta*, **1834**, 1155-1167.

30. Christensen, S.K., Maenhaut-Michel, G., Mine, N., Gottesman, S., Gerdes, K. and Van Melderen, L. (2004) Overproduction of the Lon protease triggers inhibition of translation in Escherichia coli: involvement of the yefM-yoeB toxin-antitoxin system. *Molecular microbiology*, **51**, 1705-1717.
31. Ramage, H.R., Connolly, L.E. and Cox, J.S. (2009) Comprehensive functional analysis of Mycobacterium tuberculosis toxin-antitoxin systems: implications for pathogenesis, stress responses, and evolution. *PLoS genetics*, **5**, e1000767.
32. Cooper, C.R., Daugherty, A.J., Tachdjian, S., Blum, P.H. and Kelly, R.M. (2009). Portland Press Limited.
33. Sala, A., Bordes, P. and Genevaux, P. (2014) Multiple Toxin-Antitoxin Systems in Mycobacterium tuberculosis. *Toxins*, **6**, 1002.
34. Arcus, V.L., Bäckbro, K., Roos, A., Daniel, E.L. and Baker, E.N. (2004) Distant structural homology leads to the functional characterization of an archaeal PIN domain as an exonuclease. *Journal of Biological Chemistry*, **279**, 16471-16478.
35. Arcus, V.L., Rainey, P.B. and Turner, S.J. (2005) The PIN-domain toxin–antitoxin array in mycobacteria. *Trends in Microbiology*, **13**, 360-365.
36. Daines, D.A., Wu, M.H. and Yuan, S.Y. (2007) VapC-1 of nontypeable Haemophilus influenzae is a ribonuclease. *Journal of bacteriology*, **189**, 5041-5048.
37. Robson, J., McKenzie, J.L., Cursons, R., Cook, G.M. and Arcus, V.L. (2009) The vapBC operon from Mycobacterium smegmatis is an autoregulated toxin–antitoxin module that controls growth via inhibition of translation. *Journal of molecular biology*, **390**, 353-367.
38. Makarova, K.S., Wolf, Y.I. and Koonin, E.V. (2009) Comprehensive comparative-genomic analysis of type 2 toxin-antitoxin systems and related mobile stress response systems in prokaryotes. *Biology direct*, **4**, 19.
39. Gerdes, K., Christensen, S.K. and Løbner-Olesen, A. (2005) Prokaryotic toxin–antitoxin stress response loci. *Nature Reviews Microbiology*, **3**, 371.
40. Helaine, S., Cheverton, A.M., Watson, K.G., Faure, L.M., Matthews, S.A. and

Holden, D.W. (2014) Internalization of Salmonella by Macrophages Induces Formation of Nonreplicating Persisters. *Science*, **343**, 204-208.

41. Kang, S.-M., Kim, D.-H., Lee, K.-Y., Park, S.J., Yoon, H.-J., Lee, S.J., Im, H. and Lee, B.-J. (2017) Functional details of the Mycobacterium tuberculosis VapBC26 toxin-antitoxin system based on a structural study: insights into unique binding and antibiotic peptides. *Nucleic acids research*, **45**, 8564-8580.
42. Lee, I.-G., Lee, S.J., Chae, S., Lee, K.-Y., Kim, J.-H. and Lee, B.-J. (2015) Structural and functional studies of the Mycobacterium tuberculosis VapBC30 toxin-antitoxin system: implications for the design of novel antimicrobial peptides. *Nucleic acids research*, **43**, 7624-7637.
43. Otwinowski, Z. and Minor, W. (1997), *Methods in enzymology*. Elsevier, Vol. 276, pp. 307-326.
44. Kabsch, W. (2010) XDS. *Acta Crystallographica Section D*, **66**, 125-132.
45. Krissinel, E. and Henrick, K. (2007) Inference of macromolecular assemblies from crystalline state. *J Mol Biol*, **372**, 774-797.
46. Dolinsky, T.J., Nielsen, J.E., McCammon, J.A. and Baker, N.A. (2004) PDB2PQR: an automated pipeline for the setup of Poisson–Boltzmann electrostatics calculations. *Nucleic acids research*, **32**, W665-W667.
47. Baker, N.A., Sept, D., Joseph, S., Holst, M.J. and McCammon, J.A. (2001) Electrostatics of nanosystems: application to microtubules and the ribosome. *Proceedings of the National Academy of Sciences*, **98**, 10037-10041.
48. DeLano, W.L. (2002) The PyMOL molecular graphics system.
49. Dienemann, C., Bøggild, A., Winther, K.S., Gerdes, K. and Brodersen, D.E. (2011) Crystal structure of the VapBC toxin–antitoxin complex from Shigella flexneri reveals a hetero-octameric DNA-binding assembly. *Journal of molecular biology*, **414**, 713-722.
50. Maté, M.J., Vincentelli, R., Foos, N., Raoult, D., Cambillau, C. and Ortiz-Lombardía, M. (2011) Crystal structure of the DNA-bound VapBC2 antitoxin/toxin pair from Rickettsia felis. *Nucleic acids research*, **40**, 3245-

3258.

51. Bendtsen, K.L., Xu, K., Luckmann, M., Winther, K.S., Shah, S.A., Pedersen, C.N. and Brodersen, D.E. (2016) Toxin inhibition in C. crescentus VapBC1 is mediated by a flexible pseudo-palindromic protein motif and modulated by DNA binding. *Nucleic acids research*, **45**, 2875-2886.
52. Mattison, K., Wilbur, J.S., So, M. and Brennan, R.G. (2006) Structure of FitAB from Neisseria gonorrhoeae bound to DNA reveals a tetramer of toxin-antitoxin heterodimers containing pin domains and ribbon-helix-helix motifs. *Journal of Biological Chemistry*, **281**, 37942-37951.
53. Das, U., Pogenberg, V., Subhramanyam, U.K.T., Wilmanns, M., Gourinath, S. and Srinivasan, A. (2014) Crystal structure of the VapBC-15 complex from Mycobacterium tuberculosis reveals a two-metal ion dependent PIN-domain ribonuclease and a variable mode of toxin–antitoxin assembly. *Journal of structural biology*, **188**, 249-258.
54. Holm, L. and Rosenstrï¿ ½m, P.i. (2010) Dali server: conservation mapping in 3D. *Nucleic acids research*, **38**, W545-W549.
55. Dienemann, C., Boggild, A., Winther, K.S., Gerdes, K. and Brodersen, D.E. (2011) Crystal structure of the VapBC toxin-antitoxin complex from Shigella flexneri reveals a hetero-octameric DNA-binding assembly. *J Mol Biol*, **414**, 713-722.
56. Mattison, K., Wilbur, J.S., So, M. and Brennan, R.G. (2006) Structure of FitAB from Neisseria gonorrhoeae bound to DNA reveals a tetramer of toxin-antitoxin heterodimers containing pin domains and ribbon-helix-helix motifs. *J Biol Chem*, **281**, 37942-37951.
57. Das, U., Pogenberg, V., Subhramanyam, U.K., Wilmanns, M., Gourinath, S. and Srinivasan, A. (2014) Crystal structure of the VapBC-15 complex from Mycobacterium tuberculosis reveals a two-metal ion dependent PIN-domain ribonuclease and a variable mode of toxin-antitoxin assembly. *J Struct Biol*, **188**, 249-258.
58. Miallau, L., Faller, M., Chiang, J., Arbing, M., Guo, F., Cascio, D. and Eisenberg, D. (2009) Structure and proposed activity of a member of the VapBC family of toxin-antitoxin systems VapBC-5 from Mycobacterium

tuberculosis. *Journal of Biological Chemistry*, **284**, 276-283.

59. Min, A.B., Miallau, L., Sawaya, M.R., Habel, J., Cascio, D. and Eisenberg, D. (2012) The crystal structure of the Rv0301-Rv0300 VapBC-3 toxin—antitoxin complex from M. tuberculosis reveals a Mg2+ ion in the active site and a putative RNA-binding site. *Protein Science*, **21**, 1754-1767.
60. Yamaguchi, Y., Park, J.-H. and Inouye, M. (2011) Toxin-antitoxin systems in bacteria and archaea. *Annual review of genetics*, **45**, 61-79.
61. Coburn, B., Grassl, G.A. and Finlay, B.B. (2007) Salmonella, the host and disease: a brief review. *Immunology and cell biology*, **85**, 112-118.
62. Fabrega, A. and Vila, J. (2013) Salmonella enterica serovar Typhimurium skills to succeed in the host: virulence and regulation. *Clinical microbiology reviews*, **26**, 308-341.
63. Crump, J.A. and Mintz, E.D. (2010) Global trends in typhoid and paratyphoid Fever. *Clinical infectious diseases : an official publication of the Infectious Diseases Society of America*, **50**, 241-246.
64. Crump, J.A., Griffin, P.M. and Angulo, F.J. (2002) Bacterial contamination of animal feed and its relationship to human foodborne illness. *Clinical infectious diseases : an official publication of the Infectious Diseases Society of America*, **35**, 859-865.
65. Baumler, A.J. (1997) The record of horizontal gene transfer in Salmonella. *Trends in microbiology*, **5**, 318-322.
66. Mathur, R., Oh, H., Zhang, D., Park, S.-G., Seo, J., Koblansky, A., Hayden, M.S. and Ghosh, S. (2012) A Mouse Model of< i> Salmonella</i> Typhi Infection. *Cell*, **151**, 590-602.
67. De la Cruz, M.A., Zhao, W., Farenc, C., Gimenez, G., Raoult, D., Cambillau, C., Gorvel, J.P. and Meresse, S. (2013) A toxin-antitoxin module of Salmonella promotes virulence in mice. *PLoS pathogens*, **9**, e1003827.
68. Yamaguchi, Y. and Inouye, M. (2011) Regulation of growth and death in Escherichia coli by toxin–antitoxin systems. *Nat Rev Micro*, **9**, 779-790.
69. Pandey, D.P. and Gerdes, K. (2005) Toxin–antitoxin loci are highly abundant in free-living but lost from host-associated prokaryotes. *Nucleic Acids Research*, **33**, 966-976.

70. Gerdes, K., Christensen, S.K. and Lobner-Olesen, A. (2005) Prokaryotic toxin-antitoxin stress response loci. *Nat Rev Micro*, **3**, 371-382.
71. Gerdes, K. (2000) Toxin-antitoxin modules may regulate synthesis of macromolecules during nutritional stress. *Journal of bacteriology*, **182**, 561-572.
72. McClelland, M., Sanderson, K.E., Spieth, J., Clifton, S.W., Latreille, P., Courtney, L., Porwollik, S., Ali, J., Dante, M., Du, F. *et al.* (2001) Complete genome sequence of Salmonella enterica serovar Typhimurium LT2. *Nature*, **413**, 852-856.
73. Otwinowski, Z. and Minor, W. (1997) Processing of X-ray diffraction data collected in oscillation mode. *Method Enzymol*, **276**, 307-326.
74. Adams, P.D., Afonine, P.V., Bunkoczi, G., Chen, V.B., Davis, I.W., Echols, N., Headd, J.J., Hung, L.W., Kapral, G.J., Grosse-Kunstleve, R.W. *et al.* (2010) PHENIX: a comprehensive Python-based system for macromolecular structure solution. *Acta Crystallogr D*, **66**, 213-221.
75. Emsley, P., Lohkamp, B., Scott, W.G. and Cowtan, K. (2010) Features and development of Coot. *Acta crystallographica. Section D, Biological crystallography*, **66**, 486-501.
76. Vagin, A.A., Steiner, R.A., Lebedev, A.A., Potterton, L., McNicholas, S., Long, F. and Murshudov, G.N. (2004) REFMAC5 dictionary: organization of prior chemical knowledge and guidelines for its use. *Acta crystallographica. Section D, Biological crystallography*, **60**, 2184-2195.
77. Brunger, A.T. (1992) Free R value: a novel statistical quantity for assessing the accuracy of crystal structures. *Nature*, **355**, 472-475.
78. Chen, V.B., Arendall, W.B., 3rd, Headd, J.J., Keedy, D.A., Immormino, R.M., Kapral, G.J., Murray, L.W., Richardson, J.S. and Richardson, D.C. (2010) MolProbity: all-atom structure validation for macromolecular crystallography. *Acta crystallographica. Section D, Biological crystallography*, **66**, 12-21.
79. Krissinel, E. and Henrick, K. (2004) Secondary-structure matching (SSM), a new tool for fast protein structure alignment in three dimensions. *Acta crystallographica. Section D, Biological crystallography*, **60**, 2256-2268.

80. Tina, K.G., Bhadra, R. and Srinivasan, N. (2007) PIC: Protein Interactions Calculator. *Nucleic Acids Res*, **35**, W473-476.
81. Holm, L. and Rosenstrom, P. (2010) Dali server: conservation mapping in 3D. *Nucleic acids research*, **38**, W545-549.
82. Yang, J., Zhou, K., Liu, P., Dong, Y., Gao, Z., Zhang, J. and Liu, Q. (2016) Structural insight into the E. coli HigBA complex. *Biochem Biophys Res Commun*, **478**, 1521-1527.
83. Francuski, D. and Saenger, W. (2009) Crystal structure of the antitoxin-toxin protein complex RelB-RelE from Methanococcus jannaschii. *J Mol Biol*, **393**, 898-908.
84. Liang, Y., Gao, Z., Wang, F., Zhang, Y., Dong, Y. and Liu, Q. (2014) Structural and functional characterization of Escherichia coli toxin-antitoxin complex DinJ-YafQ. *J Biol Chem*, **289**, 21191-21202.
85. Takagi, H., Kakuta, Y., Okada, T., Yao, M., Tanaka, I. and Kimura, M. (2005) Crystal structure of archaeal toxin-antitoxin RelE-RelB complex with implications for toxin activity and antitoxin effects. *Nature structural & molecular biology*, **12**, 327-331.
86. Schureck, M.A., Maehigashi, T., Miles, S.J., Marquez, J., Cho, S.E., Erdman, R. and Dunham, C.M. (2014) Structure of the Proteus vulgaris HigB-(HigA)2-HigB toxin-antitoxin complex. *J Biol Chem*, **289**, 1060-1070.
87. Kwon, A.-R. and Lee, B.-J. (1834) Crystal structure of apo and copper bound HP0894 toxin from Helicobacter pylori 26695 and insight into mRNase activity. *Biochimica et biophysica acta*, **2013**, 2579-2590.
88. Boggild, A., Sofos, N., Andersen, K.R., Feddersen, A., Easter, A.D., Passmore, L.A. and Brodersen, D.E. (2012) The crystal structure of the intact E. coli RelBE toxin-antitoxin complex provides the structural basis for conditional cooperativity. *Structure*, **20**, 1641-1648.
89. Kamada, K. and Hanaoka, F. (2005) Conformational change in the catalytic site of the ribonuclease YoeB toxin by YefM antitoxin. *Mol Cell*, **19**, 497-509.
90. Li, G.-Y., Zhang, Y., Inouye, M. and Ikura, M. (2009) Inhibitory mechanism of E. coli RelE/RelB toxin/antitoxin module involves a helix displacement

near a mRNA interferase active site. *Journal of Biological Chemistry*.

91. McGeehan, J.E., Streeter, S.D., Papapanagiotou, I., Fox, G.C. and Kneale, G.G. (2005) High-resolution crystal structure of the restriction-modification controller protein C.AhdI from Aeromonas hydrophila. *Journal of molecular biology*, **346**, 689-701.
92. Watkins, D., Mohan, S., Koudelka, G.B. and Williams, L.D. (2010) Sequence recognition of DNA by protein-induced conformational transitions. *Journal of molecular biology*, **396**, 1145-1164.
93. Kozlowicz, B.K., Shi, K., Gu, Z.Y., Ohlendorf, D.H., Earhart, C.A. and Dunny, G.M. (2006) Molecular basis for control of conjugation by bacterial pheromone and inhibitor peptides. *Molecular microbiology*, **62**, 958-969.
94. Newman, J.A., Rodrigues, C. and Lewis, R.J. (2013) Molecular basis of the activity of SinR protein, the master regulator of biofilm formation in Bacillus subtilis. *The Journal of biological chemistry*, **288**, 10766-10778.
95. Brown, B.L., Grigoriu, S., Kim, Y., Arruda, J.M., Davenport, A., Wood, T.K., Peti, W. and Page, R. (2009) Three dimensional structure of the MqsR: MqsA complex: a novel TA pair comprised of a toxin homologous to RelE and an antitoxin with unique properties. *PLoS pathogens*, **5**, e1000706.

국문 초록

살모넬라 유래의 VapBC 와 SehAB 독소-항독소 단백질의 구조적 기능적 연구

박 동 원

약학과, 물리약학 전공

서울대학교 대학원

세균성의 독소-항독소 시스템은 영양부족, 항생제 처리, 산화스트레스 등의 세포가 힘든 환경에 처했을 때 세포의 유지에 필수적인 역할을 하는 것으로 알려져 주목받고 있다. 독소-항독소 시스템은 항독소의 독소 저해 방식 혹은 항독소의 형태에 따라 6가지 독소-항독소 시스템이 존재한다. 그 중에서 타입 2 독소-항독소 시스템은 가장 많이 연구가 진행되었다. 타입 2 독소-항독소 시스템은 상대적으로 불안정한 항독소

단백질과 안정적인 독소 단백질로 구성되어 있다. 세포가 안정적인 환경에서는 독소와 항독소는 복합체를 형성하고 있지만 세포가 산화스트레스, 온도변화, 영양부족, 항생제 처리 등의 척박한 환경에 놓이게 되면 특정 단백 분해 효소에 의해 상대적으로 불안정한 항독소가 분해되고 유리된 독소는 특정 RNA를 분해하는 등의 활성을 나타냄으로써 세포가 사멸하거나 혹은 생장이 멈춘다. 타입 2 독소-항독소 시스템의 항독소의 구조에는 DNA와 결합하는 도메인이 포함되어 있는데, DNA와 결합하는 도메인을 통해 프로모터 지역의 특정 서열과 결합하여 독소와 항독소의 전사를 조절한다. 이러한 타입 2 독소-항독소 시스템의 특성은 새로운 항생제 타겟으로 주목받고 있다. 병원성 균인 살모넬라 티피뮤리엄에는 최소 14개의 타입 2 독소-항독소 시스템이 존재하며 이제까지 밝혀진 구조는 없다.

우리는 이번 연구를 통해 VapBC 독소-항독소 복합체 구조를 결정화를 통해 DNA와 결합하지 않은 그리고 결합한 구조를 각각 2 Å 그리고 2.8 Å 으로 구하였다. VapC 독소는 구조 속에 PIN domain (pilT N-terminal domain) 을 가지고 있다. PIN domain을 가지고 있는 VapC 독소는 금속 의존적 RNA 분해 능을 가진다. 또한 구조적으로 음전하를 띤 잔기들을 활성 부위에 가지고 있다. 선행된 VapBC 연구에서 기존의

VapC 독소는 마그네슘 혹은 망간 의존적인 RNA 분해 능을 보인다고 보고되었다. 하지만 우리는 처음으로 칼슘 의존적인 RNA 분해 능을 보이는 VapC 독소 단백질을 발견하였다. VapB 항독소 단백질에는 N 말단에 Abr-B DNA 결합 domain을 가지고 있으며 이 DNA 결합 domain이 프로모터 지역의 특정 서열과 결합하여 VapBC 복합체의 전사를 조절한다. DNA와 결합된 VapBC 구조를 통하여 VapB 항독소가 DNA와 결합하는 형태와 결합에 관여하는 잔기를 관찰할 수 있었다.

또한 SehAB 복합체의 구조를 결정화를 통해 2.49 Å 으로 구하였다. SehA 독소는 RelE 독소 계열로 알려져 있으며, RelE 독소는 리보솜 의존적인 RNA분해능을 보인다. SehA 독소는 RelE 계열의 독소이므로 RNA 분해 능을 보일 것으로 예상되어, 형광-퀜처 실험을 이용하여 RNA 분해 능을 측정해본 결과 SehA 독소의 C 말단 알파 나선이 독소의 활성에 영향을 준다는 것을 밝힐 수 있었다. SehB 항독소는 C 말단에 DNA 결합 도메인인 Helix-Turn-Helix를 가지고 있다. SehAB 복합체의 구조를 통해서 SehB 항독소와 SehA 항독소의 결합에 관여하는 잔기들을 관찰 할 수 있었고, SehB 항독소가 SehA 독소를 제어하는 방식을 관찰할 수 있었다.

본 연구에서는 DNA와 결합한 VapBC와 결합하지 않은 VapBC 구조를 관찰할 수 있었고, 이 구조를 근거로 VapB 항독소의 VapC 독소 제어를 관찰할 수 있었다. DNA와 결합한 VapBC 복합체 구조를 바탕으로 여러 균주 유래의 VapBC를 포함한 VapBC 복합체의 전반적인 DNA와의 결합 양상 관찰할 수 있었다. 또한, 처음으로 칼슘 의존적인 RNA 분해 능을 보인 VapC 독소를 밝혀내었다. DNA와 결합한 VapBC 복합체 구조는 현재까지 두 개의 균주에서 유래한 구조만 보고되었으며, 또한 칼슘 의존적 RNA분해능을 보이는 VapC는 처음으로 보고되었다. 이번 연구에서 밝힌 결과들은 향후 VapBC 연구의 발전에 기여할 것이다.

또한, 결정화를 통해 구한 SehAB 복합체 구조를 구하였고 구해진 구조를 바탕으로 SehA 독소와 SehB 항독소의 결합에 관여하는 잔기들을 관찰할 수 있었다. 또한 RNA 분해 능 실험을 통해 SehA 독소의 RNA 분해 능에 영향을 끼치는 요소들을 규명할 수 있었다. SehAB는 유사체와 달리 SehB 항독소가 SehA 독소의 활성 부위와의 직접적인 결합 없이 SehA 독소의 활성을 제어하는 양상을 보이는데, 이러한 SehAB 만의 독특한 결합 양상은 SehAB 복합체가 연구 주제로서 충분한 의의를 지닌다는 것을 말해준다.

살모넬라 균은 현재까지도 경제적으로 발전이 더딘 국가에 널리 퍼져있으며 기존의 항생제에 대한 내성 또한 증가하고 있다. 그러므로 새로운 기전의 항생제 개발은 살모넬라균의 치료에 많은 도움을 줄 것이다. 이번 연구에서 밝힌 3가지 독소-항독소 복합체 구조는 독소-항독소의 간의 구조적, 기능적 정보를 제공하였고 또한 본 연구에서 밝힌 독소-항독소의 구조적 특징과 기능은 독소-항독소 구조를 이용한 새로운 항생 후보 물질 개발에 초석이 될 것이다.

주요 단어: 독소-항독소, DNA-단백질 복합체, 칼슘, 항생 펩타이드

학번: 2014-30569

감사의글

서울대학교 약학대학에 재학한지도 어느덧 10년이 넘었습니다. 2008년도에 입학할 당시만 해도 대학원은 언감생심 꿈도 꾸지 않았고 그저 서울대학교 약학대학에 입학했다는 사실만으로도 넘치는 행복을 느꼈습니다. 시간이 흐르고 4학년 여름방학에 처음으로 이봉진 교수님 실험실에서 특연을 했습니다. 여름 방학 시작 직후 교통사고가 발생하여 코에 상처가 난 채로 특연을 했던 것이 실험실 생활의 첫 기억입니다. 석사 과정에 있을 때만 해도 박사 과정 역시 지내다 보면 자연스레 박사 학위 또한 따라오는 것처럼 보였습니다. 만약 이렇게 힘든 것 인줄 알았다면 박사 과정을 진학하기로 결정할 때 좀 더 많은 시간을 고민할 것 그랬습니다. 박사과정을 하는 동안 그만두고 약사 하는 게 낫지 않을까라는 생각을 꽤 자주 오랫동안 했습니다. 대단한 업적을 남긴 것은 아니지만 여기까지 올 수 있었던 것은 많은 사람들의 도움 덕분입니다. 실험결과가 좋지 못하더라도 혹은 논문이 통과가 되지 않아 시간이 지체되더라도 짜증 한 번 내지 않으시고 묵묵히 기다려 주시고 언제나 응원의 말씀을 해주신 교수님께 이 자리를 빌려 진심으로 감사하다는 말씀드리고 싶습니다. 교수님께서 그 어떠한 일로도 압박을 주지 않으셨기에 여기까

지 버티고 올 수 있었습니다. 그리고 최근 몇년간 누구보다 마음 졸였을 부모님께 죄송하고 감사하다는 말씀 전하고 싶습니다. 시간이 지체되면 지체될 수록 전화를 통해 학교일에 대해 조심스레 물어보는 부모님의 목소리를 들을 때마다 걱정시켜 드려 너무 죄송했고 면목이 없었습니다. 저 못지않게 불안하고 답답하셨을 텐데 단 한번도 기대를 거두지 않으셨고 항상 그 자리에서 힘들 때면 등을 기댈 수 있게 해주어서 여기까지 올 수 있었습니다. 그리고 서울생활을 너무 잘 하고 있어 내가 크게 신경 쓸 일이 없게 해주는 동생 진이에게도 감사하다는 말을 이 자리를 빌려 전한다. 많은 말들이 입안에서 되뇌이고 머리속에 떠다니고 가슴속에 머무르지만 모두에게 그 어떤 말보다 감사하다는 말을 꼭 전하고 싶습니다. 다들 너무 감사합니다. 제가 잘 마무리할 수 있었던 것은 모두들 덕분입니다. 다시 한 번 감사합니다. 부족하지만 박사 학위를 가진 좋은 사람이 되겠습니다.